Doctoral Dissertation

Study of Morphological Difference in Hydrogel Induced Cancer Stem Cell in Synovial Sarcoma Model Cells

（滑膜肉腫モデル細胞におけるハイドロゲル誘導幹細胞の形態学的解析）

Zannatul Ferdous

Division of Soft Matter
Graduate School of Life Science
Hokkaido University

March 2023

Declaration

I hereby declare that the matter embodied in this thesis entitled “Study of Morphological Difference in Hydrogel Induced Cancer Stem Cell in Synovial Sarcoma Model Cells" is the result of investigations conducted by me under the supervision of Associate Prof. Tsuda Masumi at Laboratory of Pathology, Hokkaido University, Japan, and it has not been submitted elsewhere for the award of any degree or diploma.

In keeping with the general practice of reporting scientific observations, due acknowledgment has been made whenever the work described has been based on the findings of the other investigators. Any omission that might have occurred by oversight or error of judgment is regretted.

Zannatul Ferdous

January 5, 2023

CERTIFICATE

I hereby certify that the work described in this thesis entitled “Study of Morphological Difference in Hydrogel Induced Cancer Stem Cell in Synovial Sarcoma Model Cells” has been conducted by Ferdous Zannatul, under my supervision at the Laboratory of Pathology, Division of Soft Matter, Graduate School of Life Science, Hokkaido University, Japan.

Associate Prof. Tsuda Masumi
(Supervisor)

List of Publications

Zannatul Ferdous*, Jean-Emmanuel Clément*, Jian Ping Gong, Shinya Tanaka, Tamiki Komatsuzaki, Masumi Tsuda

Geometrical analysis identified morphological features of hydrogel-induced cancer stem cells in synovial sarcoma model cells. *Biochemical and Biophysical Research Communications* (BBRC), Volume 642, Pages 41-49, January 2023

List of Presentations

Part of this studies was presented in the following academic conferences:

1. **Zannatul Ferdous**, Masumi Tsuda, Jean-Emmanuel Clément, Jian Ping Gong, Shinya Tanaka, Tamiki Komatsuzaki, Koji Tabata

   Morphological Analysis of Hydrogel Induced Cancer Stem Cells in Synovial Sarcoma Model Cells,

   The 60th Annual Meeting of the Biophysical Society of Japan, (9.28-9.30, 2022), Hakodate Arena, Hakodate Civic Center, Hakodate (Oral) (Presentation date: 2022.9.30)

2. **Zannatul Ferdous**, Masumi Tsuda, Jean-Emmanuel Clément, Jian Ping Gong, Shinya Tanaka, Tamiki Komatsuzaki, Koji Tabata

   Morphological Analysis of Hydrogel Induced Cancer Stem Cells in Synovial Sarcoma Model Cells,

   The 60th Annual Meeting of the Biophysical Society of Japan. (9.28-9.30, 2022), Hakodate Arena, Hakodate Civic Center Hakodate City (Poster) (Presentation date: 2022.9.28)

3. **Zannatul Ferdous,** Jean-Emmanuel Clement, James Nicholas Taylor, Koji Tabata, Yoshinori Harada, Masami Tsuda, Shinya Tanaka, Jian Ping Gong, Katsumasa Fujita, Tamiki Komatsuzaki

Workflow of Raman Data Preprocessing Using Spatial-Spectral Information Designed for Line Scanning Raman Microscope

2021 Biophysical Society of Japan Hokkaido Chapter-Tohoku Chapter, online (Oral) (Presentation date: 03.09, 2022)

4. **Zannatul Ferdous**, Masumi Tsuda, Jean-Emmanuel Clément, Koji Tabata, Yusuke Ishida, Jun Suzuka, Jian Ping Gong, Shinya Tanaka, Tamiki Komatsuzaki

Analysis of Cancer Stem Cells in Sarcoma Model Cells by Deep Neural Network

The 21st RIES-HOKUDAI International Symposium (12.10-12.11, 2020), Online, Sapporo (Poster)

5. **Zannatul Ferdous**, Masumi Tsuda, Jean-Emmanuel Clément, Koji Tabata, Jian Ping Gong, Shinya Tanaka, Tamiki Komatsuzaki

Detection of Cancer Stem Cells in Sarcoma Model Cells Using Morphological Features for Developing New Diagnostics Tools

ICReDD 3rd International Symposium (2.22-2.24, 2021), Online, Sapporo2, 22 (Poster)

6. **Zannatul Ferdous**, Jean-Emmanuel Clement, James Nicholas Taylor, Koji Tabata, Yoshinori Harada, Masami Tsuda, Shinya Tanaka, Jian Ping Gong, Katsumasa Fujita, Tamiki Komatsuzaki

Gaussian Weighted Background Correction Scheme for Hyperspectral Raman Data Preprocessing

The 22nd RIES-HOKUDAI International Symposium (12.6-12.7, 2021), Online, Sapporo (Poster)

Contents

Abbreviations

BSA: bovine serum albumin.

CSC Cancer stem cells

DAPI: 4’,6-diamidino-2-phenylindole

DIC: Differential interference contrast

DMEM: Dulbecco’s modified Eagle’s medium

DN: Double network

FBS: fetal bovine serum

GAPDH: glyceraldehyde 3-phosphate dehydrogenase

HARP: hydrogel-activated reprogramming phenomena

HEPES: 4-(-2-hydroxyethyl)-piperazine-1-ethansulfonic acid

mRNA: messenger ribonucleic acid

PAMPS: poly-2-acrylamideo-2-methylpropane sulfonic acids

PBS: phosphate-buffered saline

PDMAm: poly-N,N’-dimethylacrylamide

PRC2: polycomb repressive complex 2

PS: Polystyrene

PCR: polymerase chain reaction

RNA: ribonucleic acid

RT: Room temperature

UMAP: Uniform manifold approximation and projection

UV: Ultraviolet

Chapter 1

General Introduction

1.1 Cancer stem cells

Cancer is one of the major causes of death all over the world. About 90% cancer related death are due to the metastasis cancer [1]. Radiation, Chemotherapy and/or surgery are the most common treatment of cancer. Cancer tissues are composed of the heterogenous population with small number of CSCs or Cancer stem-like cells, progenitor cells, and majority of differentiated non-CSCs. Where most cancer treatment are designed to target the rapidly dividing cancer cells, the slow-cycling quiescent CSC remain intact and cause therapy-resistance and recurrence in cancer patients. Nevertheless, the identification of CSCs remains as a challenge owing to only few markers to detect CSCs and their limited abundance less than 1%. Thus, development of more effective drugs targeting CSCs and the analyses of the characteristics should be urgent issue for complete eradication of cancer cells from human body, contributing to improvement of prognoses of cancer patients. Therefore, efficient, and reliable detection system of CSCs is necessary.

1.2 Polymer hydrogel

Polymer hydrogels are becoming a popular choice in cell biology as they offer a more physiologically relevant environment for cells. Conventional cell culture materials such as polystyrene and glass lack the ability to mimic the complex and dynamic extracellular matrices found in many soft tissues, whereas polymer hydrogels can be tailored to match these matrices in terms of mechanical, structural, and compositional properties. A recent study demonstrated that DN hydrogels composed of PAMPS and PDMAm could efficiently convert differentiated cancer cells into cancer stem cells (CSCs), a process known as the HARP phenomenon [2]. This is an important advance as it provides a new approach for understanding the behavior of CSCs in vivo. The study also showed that morphological changes and the elevation of stemness markers occurred in cancer cells when cultured on the DN hydrogel. This suggests that the

hydrogel provides a three-dimensional microenvironment that closely mimics the extracellular matrix and can support the growth and behavior of CSCs. Overall, polymer hydrogels offer a promising alternative to traditional cell culture materials and a new tool for studying cancer and other biological systems.

1.3 Cell morphology

Cell morphology contributes to diagnosis of various diseases [3], grade of cancer [4][5], disease progression [6], and treatment responses [7]. Variation in morphology linked to underlying molecular events in disease mechanism which determine the cellular response to different external stimuli such as alteration of microenvironment [5,8,9]. Morphological changes are driven by the cytoskeletal reformation in response to various external environmental changes, local information as well as different cell types [10]. Using actin cytoskeletal information along with morphological information, Mousavikhamene, Z et al. showed the morphological difference between cancer and non-cancer cells [11]. Moreover, morphological information in cancer cells has been able to show distinct metastatic characteristics in vivo where single cell colonies formed from breast cancer cell line showed different level of metastatic potential depending on their morphological features [12], and several genes associated with cell shape determinants also differ significantly between the morphologically distinct colonies. Morphological changes have also been reported for the stem cell undergoing the differentiation process in several studies [6]. In addition, morphological characteristics of stem cell also provides the characteristics of the lineage determination in their differentiation process [13-14].

1.4 Synovial sarcoma cells

Synovial sarcoma is aggressive subtype of soft tissue sarcoma accounts for approximately 10% of all soft tissue sarcoma [15,16]. The cause of this sarcoma is formation of chromosomal

translocation t(X:18; p11:q11), resulting in the fusion gene SSX-SS18. Oncoprotein SSX-SS18 is involved in chromatin remodeling leading to epigenetic changes by replacing naïve SS18, an organizing component of the SWI/SNF or BRG1/BRM-associated factor (BAF) complex. It also causes transcriptional changes by cross-linking PRC2 to activate transcription factor 2 (ATF2) [17-23]. The necessity to understand how the translocation and elevated biomarkers interact with the host is still unknown. Further research is required for development of greater understanding of these interactions and the downstream effects that occurs in synovial sarcoma. This will enable us to monitor patients for progression of disease and to develop better treatments to completely cure this subtype of soft tissue sarcoma.

1.5 Aim of the study

The aim of this study was to evaluate the impact of PAMPS gel as a culture substrate on synovial sarcoma model cells, with a focus on changes in cell morphology and the expression of stemness-associated genes. To better understand the relationship between cell morphology and stemness induction, fluorescence images of Sox2 and actin in CSCs were analyzed and single cells were segmented. Using geometrical features and unsupervised dimensional reduction, the study found a correlation between cell shape and Sox2 expression. The results show that cells with higher Sox2 expression tend to have a smaller, round shape, while flat polygonal cells have low Sox2 expression on hydrogel. In conclusion, there is a clear connection between the morphological changes in cells on hydrogel and an increase in stemness.

Chapter 2

Materials and Methods

2.1 Synthesis of PAMPS gel for cell culture

2-acrylamide-2-methyl-1-propanesulfonic acid (AMPS; Tokyo Kasei Kogyo), and 2-oxoglutaric acid (Wako Pure Chemicals, Japan) were purchased. N,N′-Methylene-bis-acrylamide (MBAA; Tokyo Kasei Kogyo) was purified by recrystallization from ethanol. PAMPS gel was synthesized by radical polymerization. An aqueous solution of 1 mol/L monomer, 4 mol.% of MBAA as crosslinker, and 0.1 mol.% 2-oxoglutaric acid as initiator were prepared in a reaction cell that had been purged with nitrogen gas for 30 min and irradiated with UV light for 10 h. All gel reactions were carried out between a pair of glass substrates, separated by a 1.0 mm thick spacer. After gelation, gels were immersed in HEPES; (Sigma) buffer solution ($NaHCO_3$ 1.55 (10^{-2} M, HEPES 5×10^{-3} M, NaCl 0.14 M, pH 7.4) and the HEPES solution was changed twice every day for 1 week to reach equilibrium [24].

After sterilizing by autoclaving (120 ℃, 20 min), gel disks were punched out of gel plate with a hole punch with a diameter of 1.5 cm. The thickness of gel was about 2–3 mm. The gel disks were then placed in 24-well polystyrene tissue culture dishes.

2.2 Cell culture

Murine myoblast cells C2C12 and its SS18-SSX1-infused cells (C2C12-SS18-SSX1 cells, synovial sarcoma model cells) were cultured in DMEM containing 10% FBS, and seeded on PAMPS gel or PS dish/glass bottom dish with density 1×10^5 cells/ml. The cultured cells were placed in an incubator at 37° C containing 5% CO_2. After 24 hours incubation, the cells were washed with PBS (-) for any further experiment. Cell morphology was observed under the light microscope.

2.3 RNA extraction and PCR expression analysis

Total RNA from cells was extracted using a RNeasy Mini Kit (Qiagen, Valencia, CA) according to the manufacturer's protocols.). RNA quality from each sample was assured by the A260/280 absorbance ratio. The RNA was reverse transcribed into cDNA using the SuperScript® VILO™ cDNA Synthesis Kit (Invitrogen, Carlsbad, CA). The sequences of primers used in real-time PCR analyses were shown in Table 2.1. Real-time PCR analysis was performed using the StepOnePlus™ Real-Time PCR System (Applied Biosystems, Waltham, MA) using Power SYBR® Green PCR Master Mix (Invitrogen). The cDNA template (10 ng) was used for real-time PCR in a final volume of 10 µl, and cDNA was amplified according to the following conditions: 95°C for 15 sec and 60°C for 1 minute at 40 amplification cycles. Relative expression levels of RNA were normalized to GAPDH and we used $2^{-\Delta\Delta Ct}$ method to obtain the value for relative mRNA expression.

Table: 2.1: Primer sequence for PCR experiment

GAPDH	
Forward Reverse	5’- TGTGTCCGTCGTGGATCTGA -3’ 5’- TTGCTGTTGAAGTCGCAGGA -3’
Nanog	
Forward Reverse	5’- CAGAAAAACCAGTGGTTGAAGACTAG -3’ 5’- GCAATGGATGCTGGGATACTC -3’
Sox2	
Forward Reverse	5’- TAGAGCTAGACTCCGGGCGATGA -3’ 5’- TTGCCTTAAACAAGACCACGAAA -3’
Oct3/4	
Forward Reverse	5’- TCTTTCCACCAGGCCCCCGGCTC -3’ 5’- TGCGGGCGGACATGGGGAGATCC -3’

2.4 Immunofluorescence

We fixed the cells with 3% paraformaldehyde in PBS for 15 min at room RT and washed with PBS. After an incubation for 20 min with 1% BSA for blocking nonspecific antibody reactivity, we washed the cells with PBS. Following that, the cells were incubated with anti-Sox2 antibody purchased from Cell Signaling Technology (Beverly, MA) [Cat# D9B8N] in concentration 1:400 diluted in PBT containing 0.1% BSA and 0.05% Triton X-100 in PBS overnight at 4°C and rinsed 3 times with PBT. After washing the primary antibody with PBT we incubate the cells with AlexaFluor594-conjugated secondary antibody (Invitrogen) with dilution concentration of 1:200 for 1 hour at RT and then rinsed with PBT 3 times. Following that it was incubated for 30 min in 37°C in dark after applying phalloidin (Alexa-488 conjugated phalloidin) with a concentration 1:50 and DAPI with concentration 0.1 mg/ml

diluted in PBS. The sample was rinsed 3 times with PBT and then replaced by PBS for imaging. Images were observed and acquired with a phase contrast microscope, and FV3000 confocal laser scanning microscope (Olympus, Tokyo, Japan). Fluorescence images was acquired using a 10× objective image at 2048 × 2048 resolution, 0.621 μm/pixel and phase contrast images was acquired with 20× objective at 1200 × 1600 resolution, 0.44 μm/pixel.

2.5 Cell segmentation

Cell image processing for obtaining the morphological features from fluorescence images was conducted using a custom-built program developed in MATLAB (MathWorks, MA). The actin-stained fluorescence images were used for cell body segmentation, and the green channel was selected for analysis. At first, intensity of the images is rescaled into range [0,1] for contrast enhancement, shown in Fig. 2.1b. We applied 0.01 as threshold to create a binary mask from the rescaled image. Binary images were filled with "imfill*"* function, image after the operation is shown in Fig. 2.1c. Then an image opening operation (using "bwareaopen*"* function in MATLAB) was performed to remove small objects defined by a threshold (500 pixels) lower than the average cell size (Fig. 2.1d). Following that, cells touching the boundary pixels were removed using MATLAB function "imclearborder" (Fig. 2.1e). Later the cells that were touching was discarded manually and labelled with individual identity as shown in Fig 2.1f.

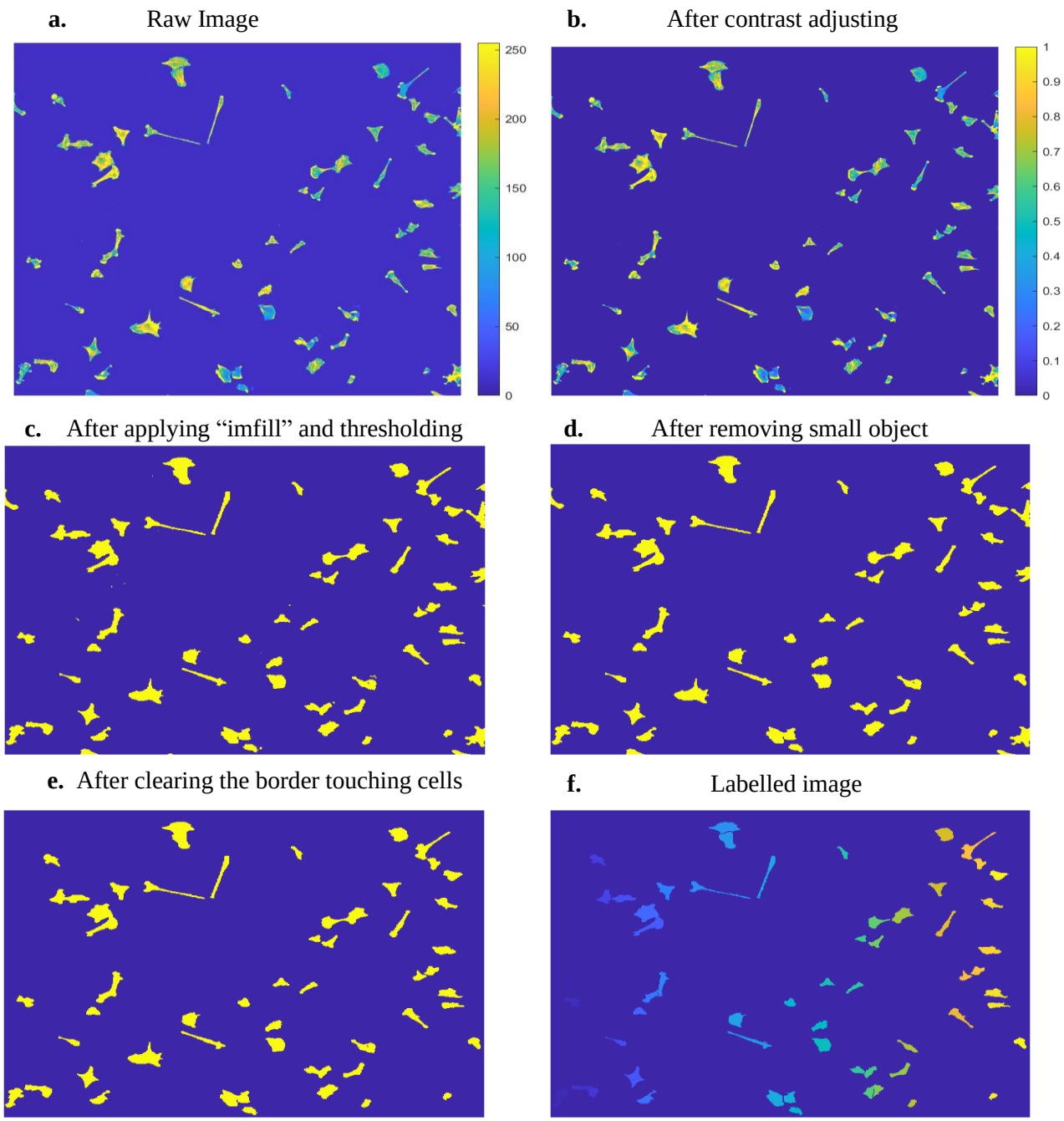

Fig. 2.1: Actin-stained image at each processing step.

(a) Raw image of Actin-stained image, scale bar indicating the raw intensity in the image, (b) Image after contrast adjustment, scale bar indicating the normalized intensity in the image, (c) Binary image after thresholding and applying filling, (d) Image after clearing the small object such as cell debris, (e) Image after removing the cells that is touching the border of the image, (f) Final image after labelling that is used for computation of individual cell shape feature.

2.6 Nucleus segmentation

Nucleus segmentation was performed on blue channel of the DAPI stained fluorescence images. At first, intensity of the images is rescaled into range [0,1] for contrast enhancement. We applied 0.35 as threshold to create a binary mask from the rescaled image followed by another operation "imfill" to fill any holes inside connected pixels. Then an image opening operation (using "bwareaopen" function in MATLAB) was performed to remove small objects defined by a threshold (200 pixels) lower than the average nucleus size. Following that, cells touching the boundary pixels were removed using MATLAB function "imclearborder". Following that individual cell was labeled using matlab function "bwlabel". Later the nuclei that were touching (Example is shown in Fig. 2.2) and the associated cell was withdrawn from the analysis. Binary mask of the nucleus was labelled with the same label as the cell body. All the operations performed for nucleus segmentation is similar to the cell segmentation steps.

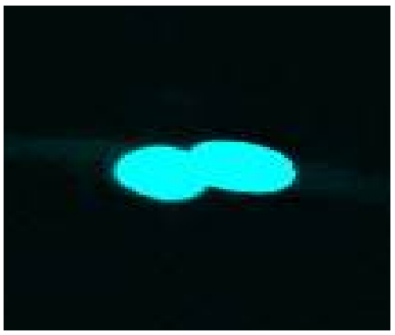

Fig. 2.2: Example image of touching nucleus

2.7 Cell shape quantification

Cells from segmented fluorescence images was labelled with a unique ID first to compute their geometrical features. A set of whole-cell shape features adopted from Ref. [25, 26] such as area, perimeter, circularity, solidity etc. were computed from each cell. The full list of features along with their description is given in Table 2.2. The whole database contains of total of 6453 cells consisting of 2259 cells from C2C12 cells on PS dish (24 images), 1068 cells from C2C12 cells on PAMPS gel (16 images), 1378 cells from C2C12 SS18-SSX1 cells on PS dish (15 images) and 1748 cells from C2C12 SS18-SSX1 cells on PAMPS gel (21 images).

Firstly, all the features $\{F_i\}$ are standardized with their means μ_i and standard deviations σ_i before any further analysis ($F_i \rightarrow (F_i - \mu_i)/\sigma_i$). The space made from 12 standardized geometrical quantities characterizes the shape of a single cell, called shape space hereinafter. The feature set was utilized to perform a UMAP projection [27] in a 2D dimensional space. For acquisition of Sox2 intensity and high contrast morphological features of single cells, the immunofluorescence images of anti-Sox2 antibody were first globally normalized [28] to adjust the contrast of different images in different conditions [29]. Afterwards, corresponding Sox2 intensity was mapped for individual cell nucleus using nucleus region segmented from DAPI stained images to compute the average intensity for each cell. Average Sox2 intensity of individual set was rescaled between [0,1] to examine how Sox2 intensity in cells within each image are distributed over the shape space of single cells. The distribution of Sox2 intensity at each operation is provided in Fig. 2.3. All the computation was performed in MATLAB R2020b version.

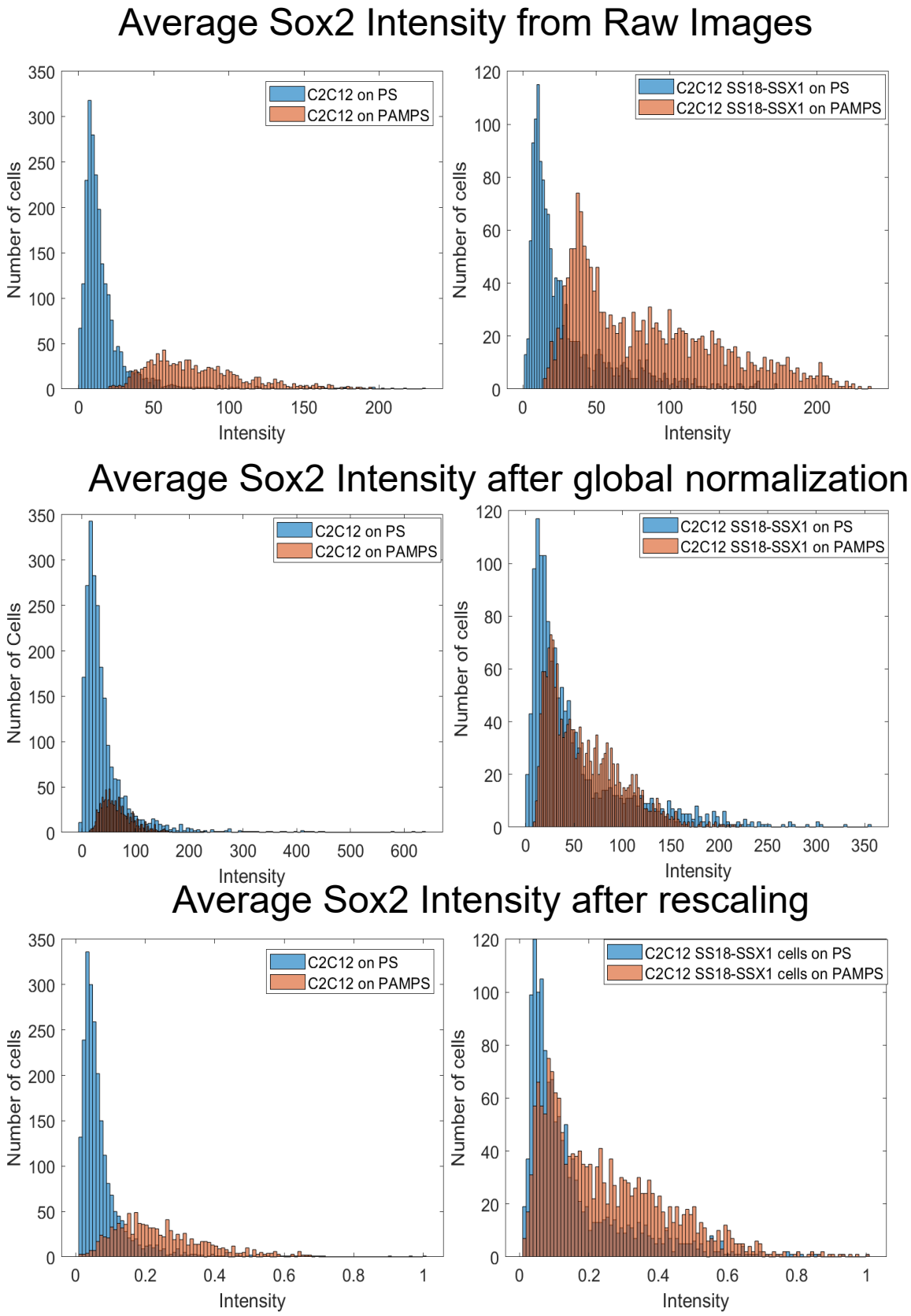

Fig. 2.3: Intensity distribution of Sox2 in each stage of image processing.

Table 2.2: Morphological features

#	Feature Name	Feature description
1	Area	Number of pixels in the cell region
2	Perimeter	Number of pixels at edge of object
3	Circularity	Circularity value for each object in the input image. The circularity value is computed as (4*Area*pi)/(Perimeter^2). For a perfect circle, the circularity value is 1.
4	Solidity	Proportion of the pixels in the convex hull that are also in the cell region. Computed as Area/Convex Area.
5	Major Axis	Length (in pixels) of the major axis of the ellipse that has the same normalized second central moments as the region.
6	Convex Area	Number of pixels in the convex polygon enclosing the cell boundary.
7	Extent	Ratio of major axis length to the cell area.
8	Aspect Ratio	Ratio between major axis length and minor axis length
9	Maximum ferret diameter	Maximum distance between two-parallel tangents on cell boundary
10	Minimum ferret diameter	Minimum distance between two-parallel tangents on cell boundary
11	Skeleton End Points	Number of endpoints of skeleton from the cell skeleton image.
12	Roughness	Roughness is computed as the ratio of average distance from cell center to the boundary to the standard deviation of the distribution of same distance.

2.8 UMAP Embedding

The UMAP algorithm [27] was used to embed the high-dimensional cellular features space into 2 dimensions for visualization. UMAP was run with an initial neighbor number of 15 and “Mahalanobis” distance as metric.

2.9 Statistical Analysis

Graphical data of PCR experiment are presented as means and standard deviation. Two tail student's *t*-test was used for comparison, with $P<0.05$ considered significant. Pearson correlation in Fig. 3.10 was computed using MATLAB function "corr", where correlation coefficient can range from -1 to +1. A value of -1 indicated perfect negative correlation, whereas a value of +1 indicated perfect positive correlation. A value of 0 indicates no correlation.

2.10 Clustering Analysis

Morphological features of cells clustered on hydrogels for both wildtype C2C12 and sarcoma model C2C12 SS18-SSX1 was clustered into 3 cluster using MATLAB in-built function "kmeans" using default distance matrix. In addition, Sox2 intensity was also clustered for the same cells using MATLAB function "kmedoids" using "Mahalanobis" distance matrix into two clusters.

Chapter 3

Results

3.1 Morphological alteration of cells on hydrogel and stemness elevation

To investigate the influence of PAMPS gel, we cultured the C2C12 cells and the C2C12-based SS18-SSX1-transformed cells (C2C12-SS18-SSX1) as synovial sarcoma model cells on the PAMPS hydrogel and PS dish. First, we observed difference in cell morphology of wildtype C2C12 cells and C2C12 SS18-SSX1 cells using phase contrast microscope. Both types of cells showed spindle shape on the PS dish (Fig. 3.1a, leftmost photo), while morphological heterogeneity was appeared in both cells on the PAMPS gel, mainly flat and spread cells on the gel surface (Fig. 3.1a, white arrowheads), elongated cells (Fig. 3.1a, black arrowheads), and round cells (Fig. 3.1a, black arrows). Time-lapse microscopic observation clarified the characteristics of each cell; the flat cells sometimes divided; the elongated spindle cells moved around vigorously, and round cells remained in place while appearing to be in contact with the gel (Movie 3.1). In concordance with their morphological change, the expression levels of cancer stemness markers such as *Sox2*, *Nanog* and *OCT3/4* were significantly increased on the PAMPS gel, which was higher in the C2C12 SS18-SSX1 cells than the wildtype cells (Fig. 3.1b). The stemness marker elevation on PAMPS gel, the first network of DN gel indicate the reprogramming phenomena that has been reported using the DN gel.

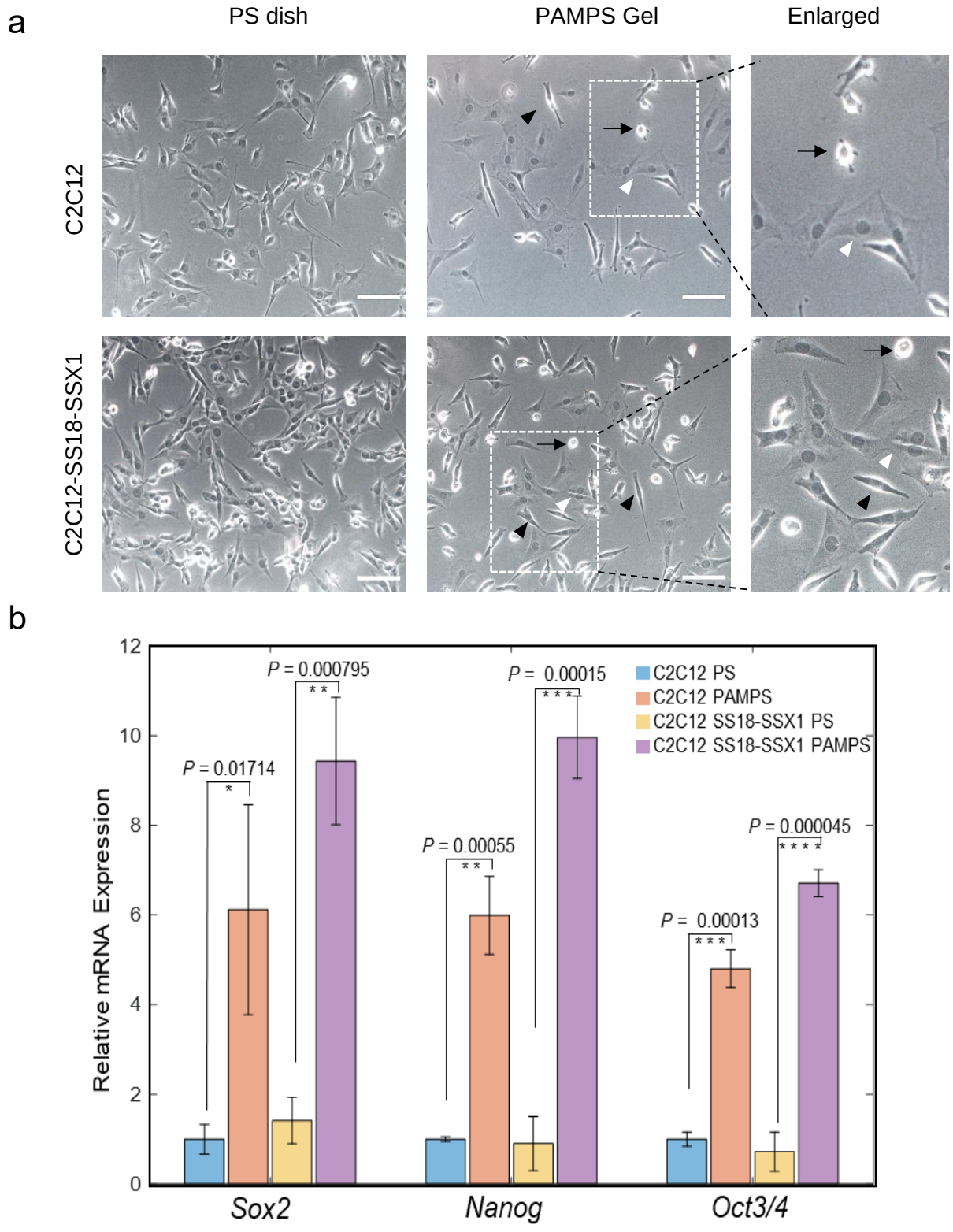

Fig. 3.1 Change of morphology and stemness elevation on hydrogel

(a) C2C12 and its SS18-SSX1-transformed cells (C2C12-SS18-SSX1) were cultured on polystyrene (PS) dish and PAMPS gel, and the phase-contrast images after 24 hours were

displayed. Some area on the PAMPS gel were magnified in the right column. white arrowheads; flat and spread cells, black arrowheads; elongated cells, and black arrows; round cells. Scale bars represent 100 μm. (b) Real-time PCR analysis of the mRNA levels of the stemness marker genes *Sox2*, *Nanog*, and *Oct3/4* in the C2C12 and C2C12-SS18-SSX1 cells cultured on PS dish and PAMPS gel for 24 hours. *P < 0.05, **P < 0.001, ***P < 0.0005, ****P < 0.00005 vs. PS. (Student's t test).

3.2 Stemness marker Sox2 is increased on PAMPS gel

To clarify the relationship between cell morphology and stemness elevation, we examined the Sox2 expression in the cells cultured on the PS dish and the PAMPS gel from immunofluorescence images, along with actin cytoskeleton and nuclear staining by phalloidin and DAPI, respectively (Fig. 3.2). We found that the spread and adherent cells on the PAMPS gel grew in clusters and exhibited quite low Sox2 expression (Fig. 3.2a, white arrowheads). In contrast, small round cells grew sparsely and had high expression of Sox2 (Fig. 3.2a, white arrows). The long or slightly elongated cells exhibited low to intermediate Sox2 expression. Only few cells on PS dish exhibited high Sox2 compared to their cultured on PAMPS gel and there seems to be no visible similarity between cell morphology and the Sox2 expression levels (Fig. 3.3). In addition, the number of high Sox2 expressing cells on PS dish was higher in C2C12 SS18-SSX1 cells than C2C12 cells. The percentage of the cells with high Sox2 on the PAMPS gel (27% and 32% in C2C12 and C2C12-SS18-SSX1 cells, respectively) was approximately five times higher compared to those on the PS dish (4.7% and 7% in C2C12 and C2C12-SS18-SSX1 cells, respectively, Fig. 3.2b). These results indicate that there is a relation between different morphological feature of the cells and the stemness elevation of the cells on hydrogel.

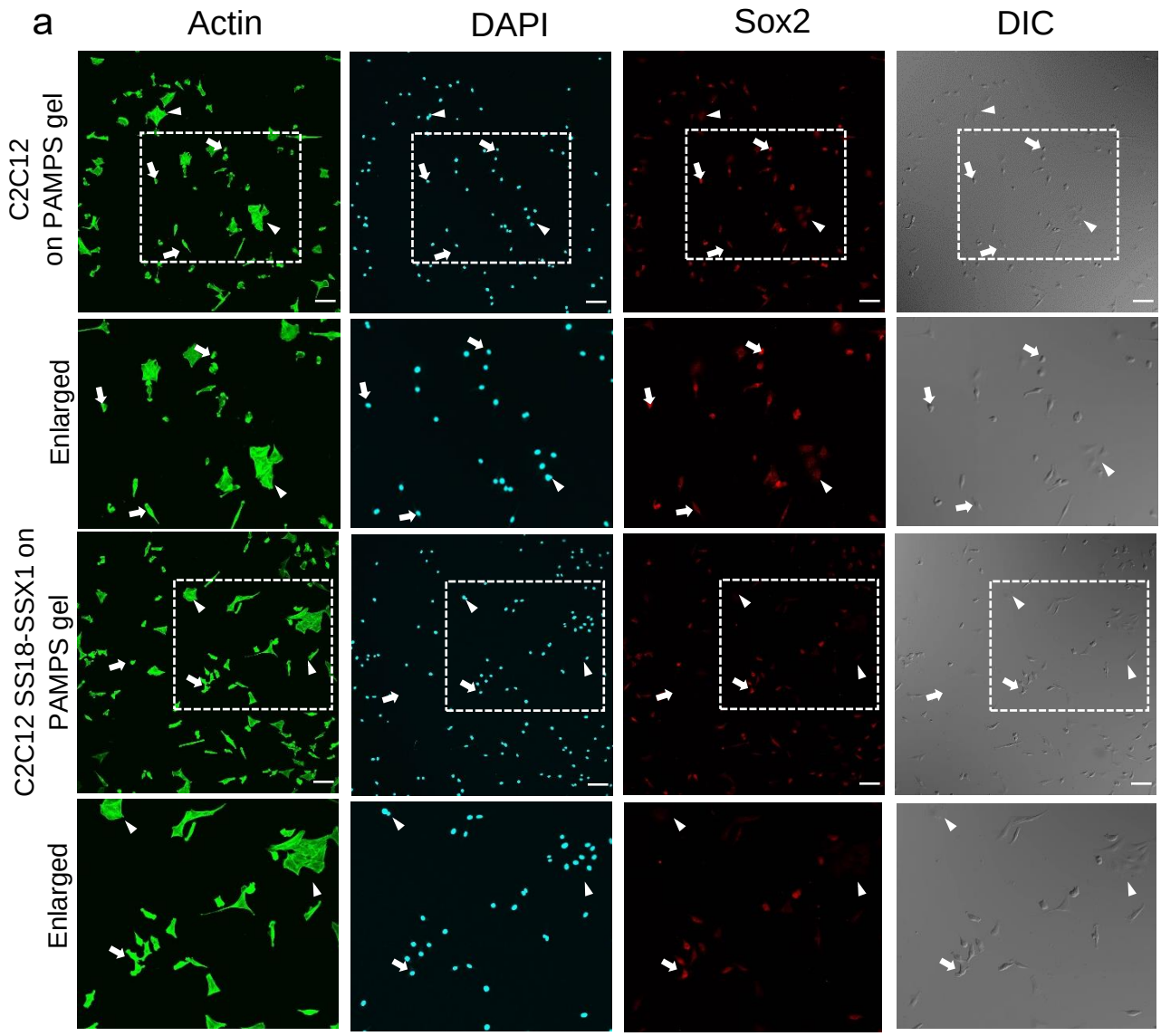
a
Actin
DAPI
Sox2
DIC
C2C12 on PAMPS gel
Enlarged
C2C12 SS18-SSX1 on PAMPS gel
Enlarged

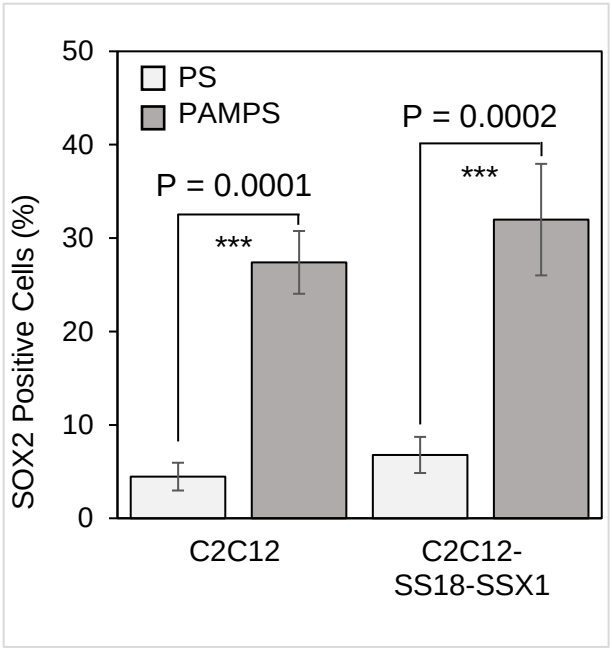
b
PS
PAMPS
P = 0.0001
P = 0.0002
***
***
SOX2 Positive Cells (%)
50
40
30
20
10
0
C2C12
C2C12-SS18-SSX1

Fig. 3.2 Immunofluorescence image revealed elevation of stemness marker on PAMPS gel.

(a) Immunofluorescence images of C2C12 and C2C12-SS18-SSX1 cells after 24 hours cultured on PAMPS gel. Actin (green), nucleus (blue), Sox2 (red), and DIC images were shown. Area in each upper panel were enlarged in the lower panels. Scale bars indicate 100 μm. (b) In C2C12 and C2C12-SS18-SSX1 cells cultured on PAMPS gel and PS dish, percentage of Sox2 positive cells were graphed (each n=5). The data represent means ± s.d.. ***$P < 0.0005$ vs. PS.

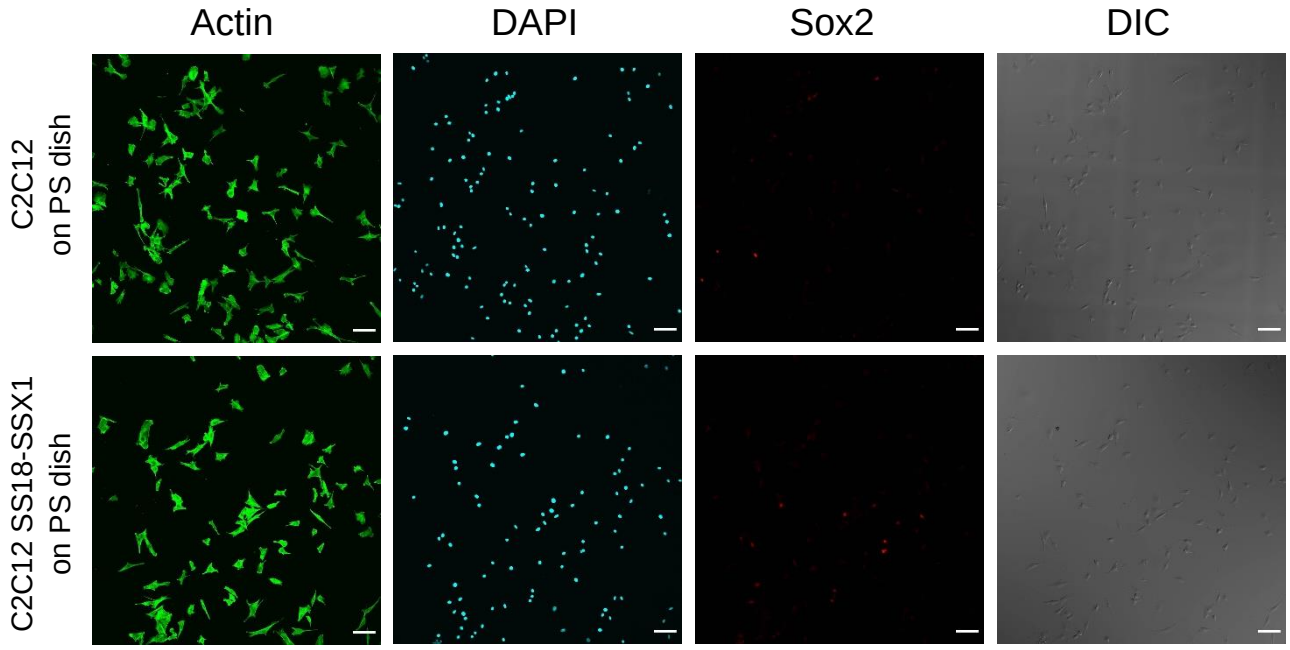

Fig 3.3: Cell morphology of the cells after 24-hour culture on PS dish.

C2C12 cells and C2C12 SS18-SSX1 cells on PS dish. Actin (green), nucleus (blue), Sox2 (red), and DIC images were shown. Area in each upper panel were enlarged in the lower panels. Scale bars indicate 100 μm.

3.3 Segmentation, feature extractions and exploration of the relation between the Sox2 expression and the cell morphology

To investigate the role of cell morphological differences to the elevation of the stemness, we examined single cell morphometrical features using unsupervised dimensional reduction simultaneously from the fluorescence images of Sox2. First, we segmented a total of over 6,400 cells from 76 fluorescent images and extracted 12 geometrical features described in Table 2.2. Using UMAP, we reduced the original 12 morphological dimension to a 2-dimentional space and showed that the morphological features can explain the cell shape in the UMAP space as cells sharing similar shape are localized close to each other in the UMAP space (Fig 3.4 - 3.7). Fig. 2.3 manifests that the raw Sox2 intensities of C2C12 and C2C12 SS18-SSX1 cells on PAMPS gel are distributed higher on average than those on PS dish. Thus, we focused on relationship between the relative Sox2 intensity of individual cells and their morphological heterogeneity only within each condition C2C12 and C2C12 SS18-SSX1 cells on PS dish/PAMPS gel (Figs. 3.8b, 3.8c) (Note that actual Sox2 intensity levels on each condition are different in Figs. 3.8b and 3.8c, and one should not compare the color of Sox2 expression level across conditions). The cells with relatively high Sox2 on the PS dish were scattered randomly in the UMAP and, importantly, had no similar morphological characteristics (Figs. 3.8b, 3.8c, 3.4, and 3.6), whereas the cell on the PAMPS gel demonstrated that cells with relatively high Sox2 expressions exhibited similar morphological characteristics (Figs. 3.8b, 3.8c, 3.5, and 3.7). Here, on the PAMPS gel, the round cells and the flat adherent cells expressed high and reduced Sox2 intensity, respectively, which was consistent with the observed morphology in Fig. 3.2a. In Fig. 3.9 we show the representative cell morphology associated to the cells cultured on PAMPS gel.

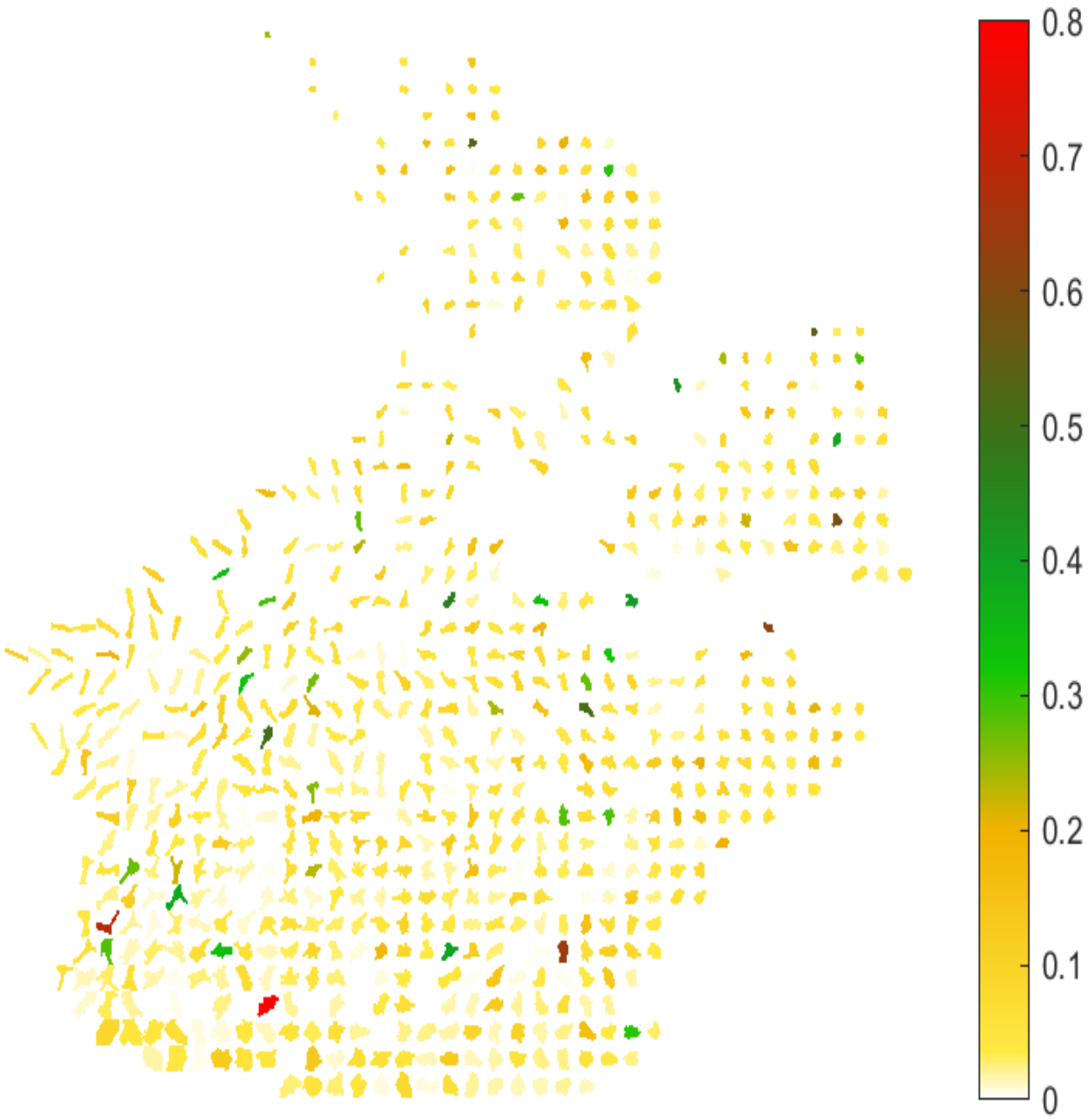

Fig 3.4: Morphology of C2C12 cells on PS dish in the UMAP space.

C2C12 cell shape projection on UMAP space from PS dish with normalized SOX2 intensity (Scale bar). Scale bar is optimized for better contrast.

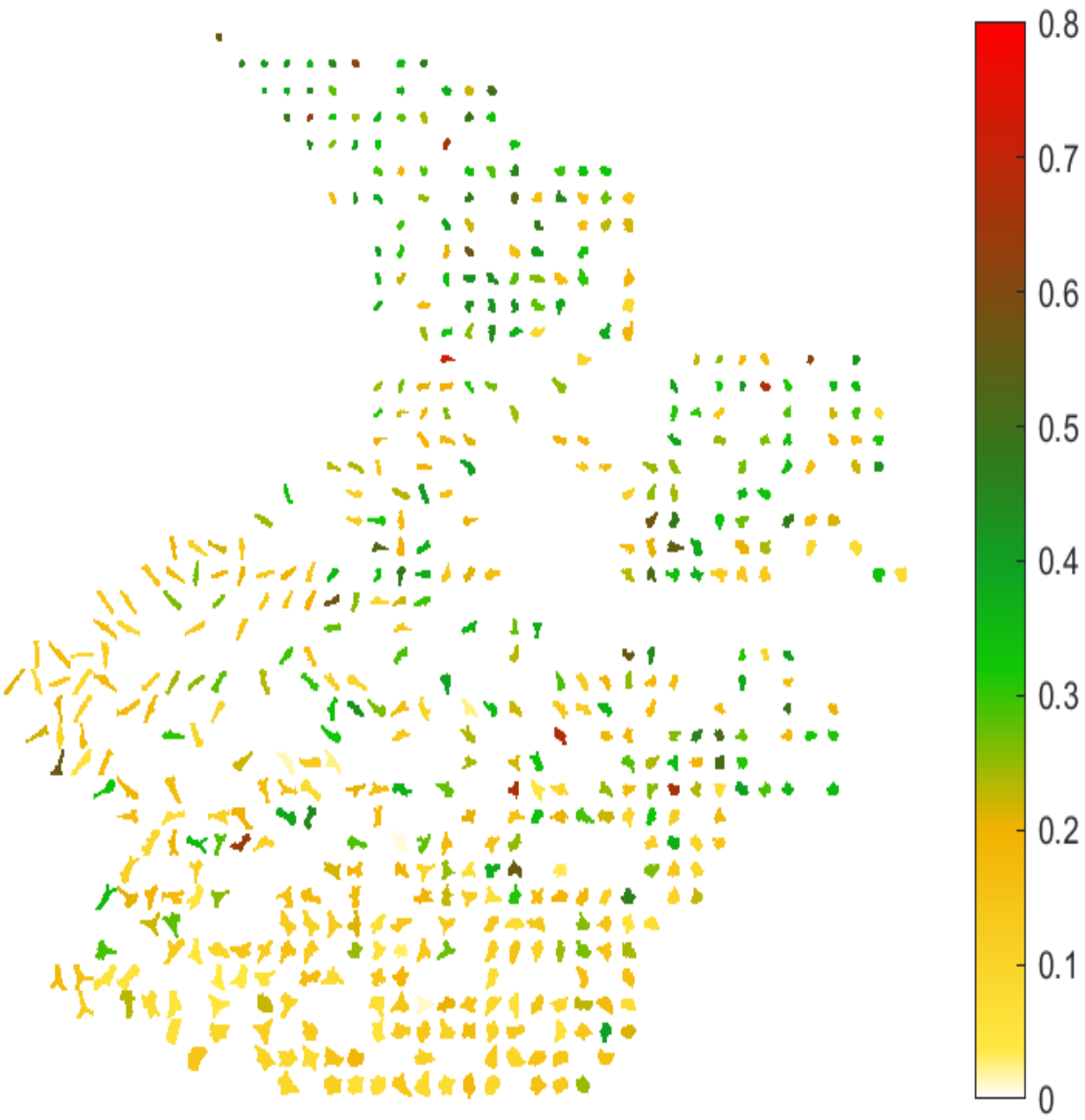

Fig 3.5: Morphology of C2C12 cells on PAMPS gel in the UMAP space.

C2C12 cell shape projection on UMAP space from PAMPS gel with normalized SOX2 intensity (Scale bar). Scale bar is optimized for better contrast.

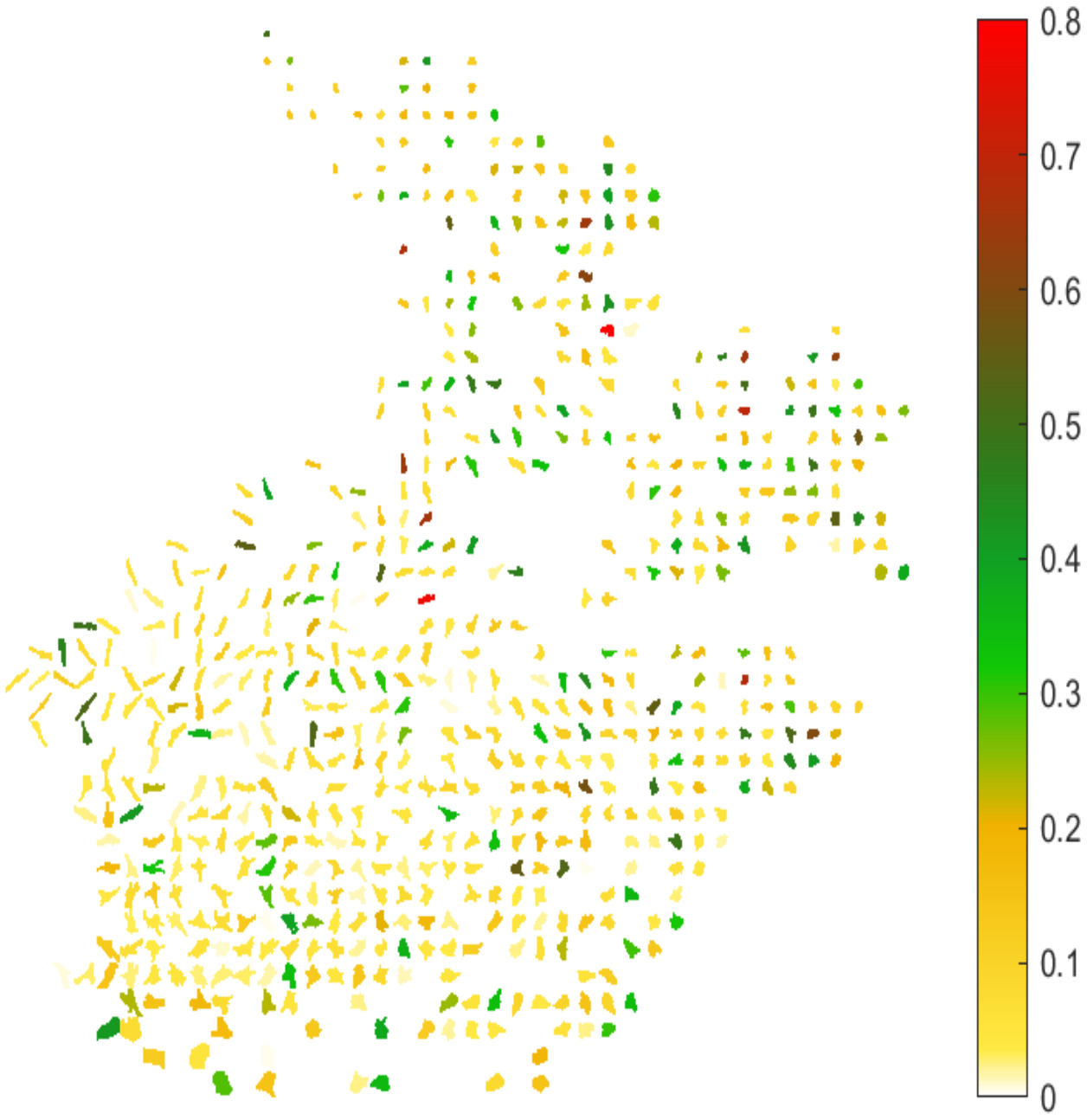

Fig. 3.6: Morphology of C2C12 SS18-SSX1 cells on PS dish in the UMAP space.

C2C12-SS18-SSX1 cell shape projection on UMAP space from PS dish with normalized SOX2 intensity (Scale bar). Scale bar is optimized for better contrast.

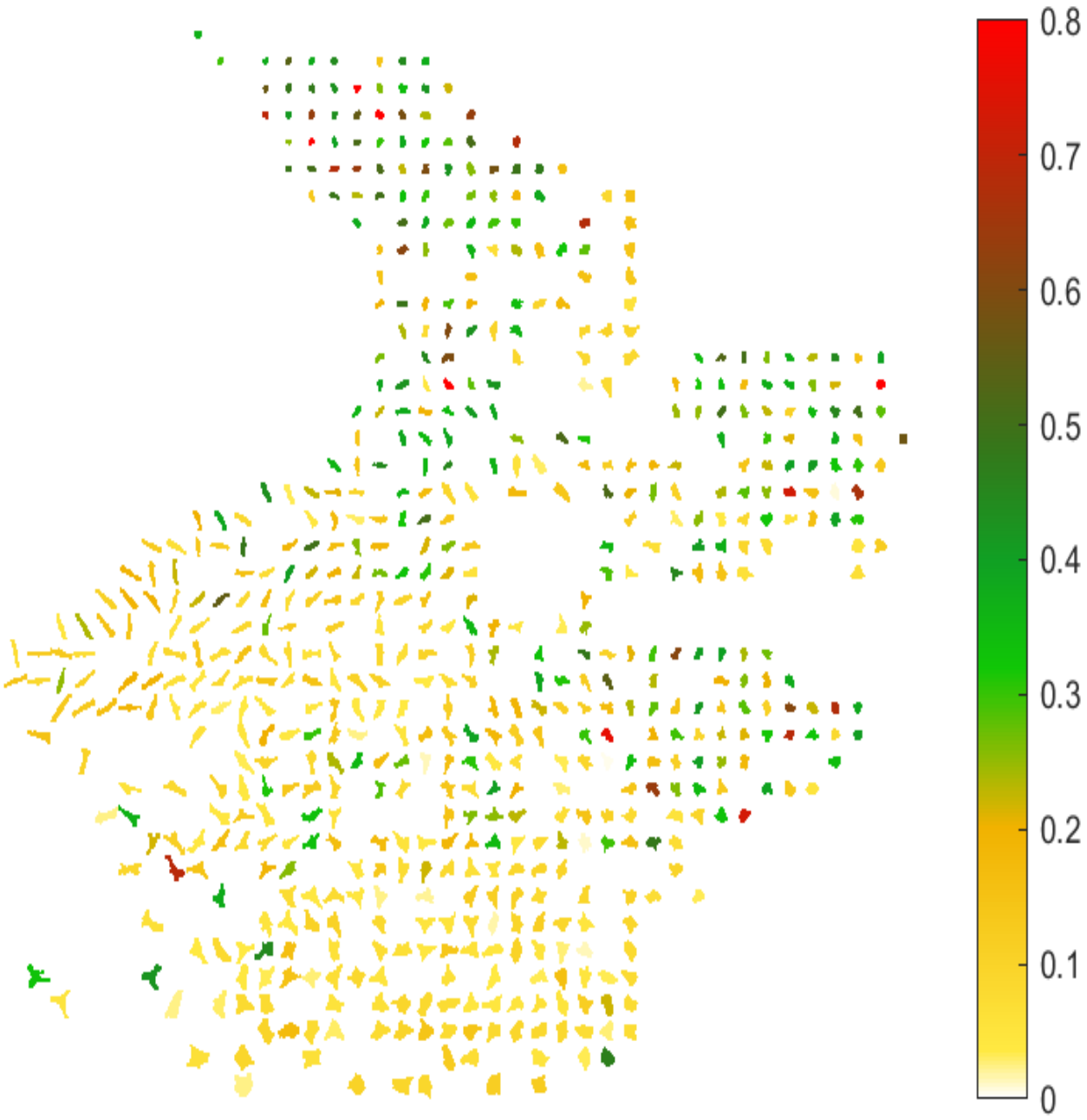

Fig. 3.7: Morphology of C2C12 SS18-SSX1 cells on PAMPS gel in the UMAP space.

C2C12-SS18-SSX1 cell shape projection on UMAP space from PAMPS gel with normalized SOX2 intensity (Scale bar). Scale bar is optimized for better contrast.

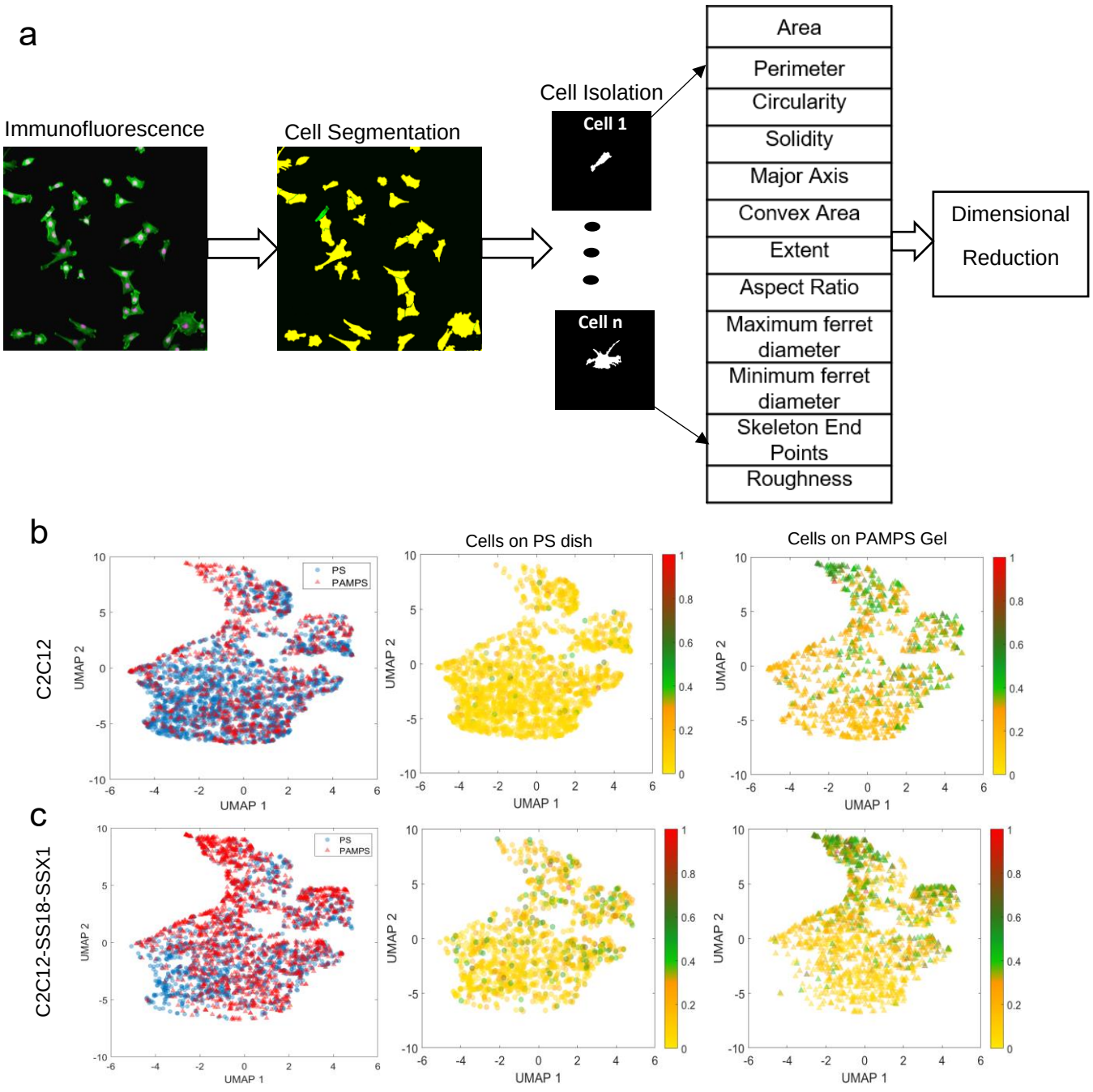

Fig. 3.8: (a) Workflow of the morphological analysis. Images of fluorescence were segmented at single cell level, and the 12 geometrical features were extracted from each cell, accompanied by dimensional reduction at the final stage (b,c) 2d-UMAP projection of the cells from different conditions. (b) C2C12 and (c) C2C12-SS18-SSX1 cells were cultured on PS dish and PAMPS gel. Color bar represents the normalized Sox2 intensity for the individual cell.

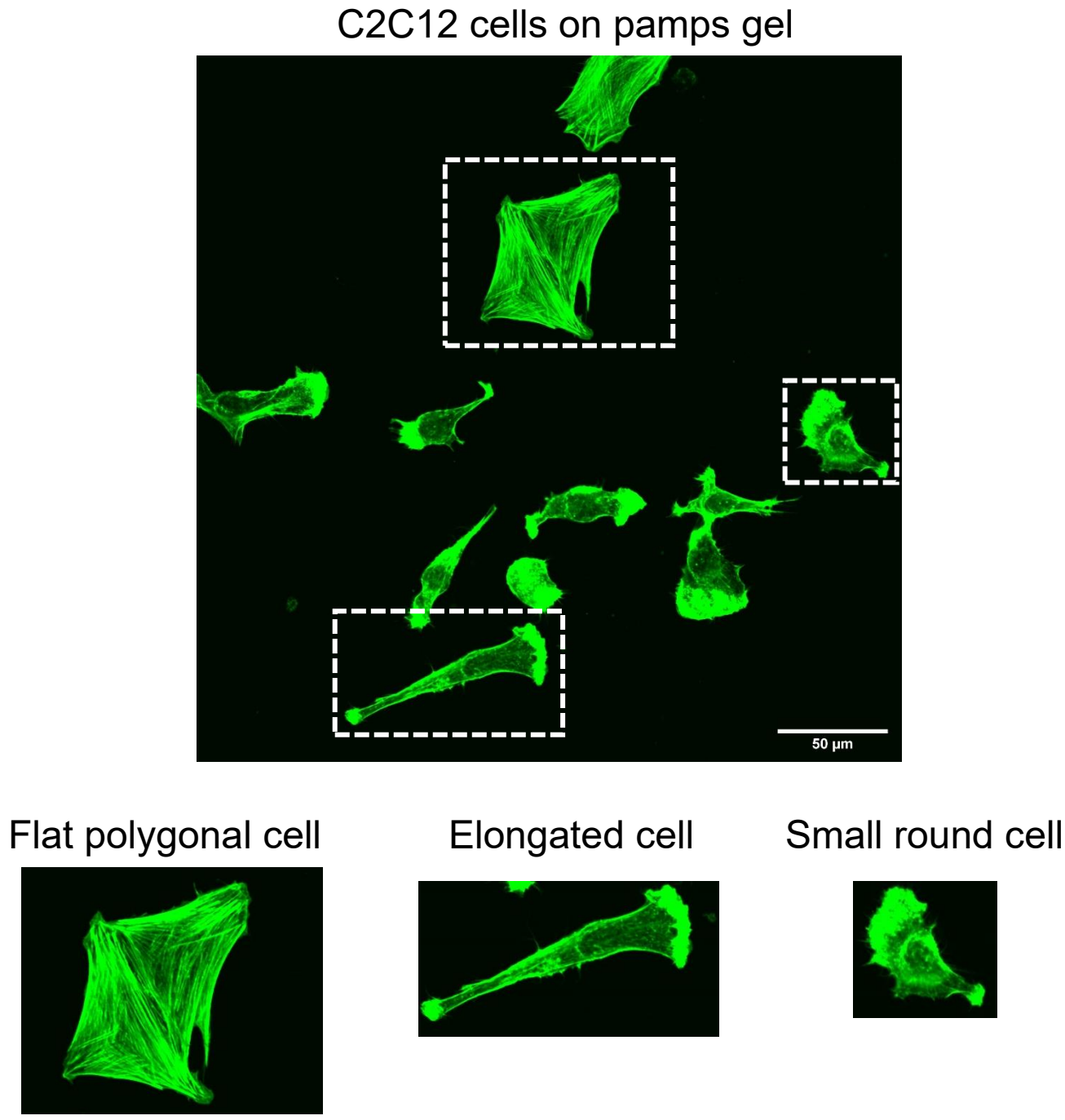

Fig. 3.9: Representative cell morphology on PAMPS gel. Scale bar represents 50 µm.

3.4 High Sox2 expressed cells on PAMPS gel and their associated morphological feature

We explored the relation between the Sox2 intensity and different morphological features for the single cell group using Pearson correlation coefficient shown in Fig. 3.10. In 12 geometrical features we tested, circularity and solidity were positively correlated with Sox2 expression, whereas perimeter and maximum ferret diameter were negatively correlated with it, this indicates the relation of morphology to the stemness expression in cells cultured on PAMPS gel, where small round cell have small perimeter and maximum ferret diameter is small as well, whereas if the cell is large or elongated the perimeter is high and also maximum ferret diameter is high, however solidity of elongated cell is smaller compared to the flat polygonal and small round cells (Figs. 3.10-3.14). Variation between distinctive features localized the cells in different position in UMAP space. The normalized value of each feature between different cell groups are shown in Fig. 3.11-3.14. This result suggests that there is strong evidence of the relation between morphological differences on the PAMPS gel-induced stemness elevation. To analyze the rates of CSCs with small round cells, the cells were clustered into 3 clusters by the 12 morphological features using k-means clustering algorithm. In C2C12 cells cultured on the PAMPS gel, cluster 1 (Figs. 3.15a, 3.16a) mainly containing small round cells with high Sox2 accounts for 61.7%, which increased to 83.2% in C2C12-SS18-SSX1 cells as sarcoma model, suggesting the synovial sarcoma model cells might be small round CSCs more readily (Figs. 3.15d, 3.16d). Together these results suggest that cells having more round morphology has a higher tendency to go through the HARP phenomena and elevate stemness associated genes on PAMPS gel.

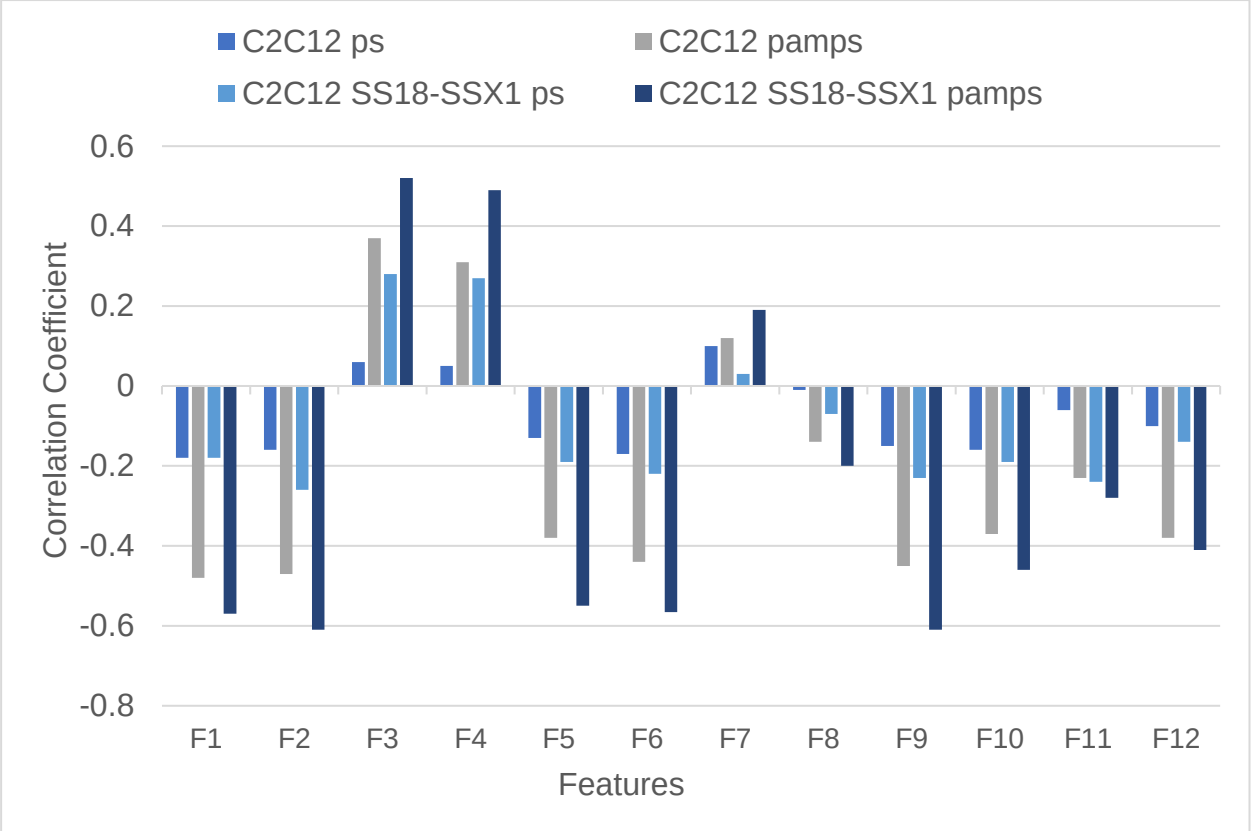

Fig. 3.10: Pearson's correlation coefficient between features and Sox2 intensity. In the graph, F1 to F12 indicate Feature 1 to 12 in Table 2.2.

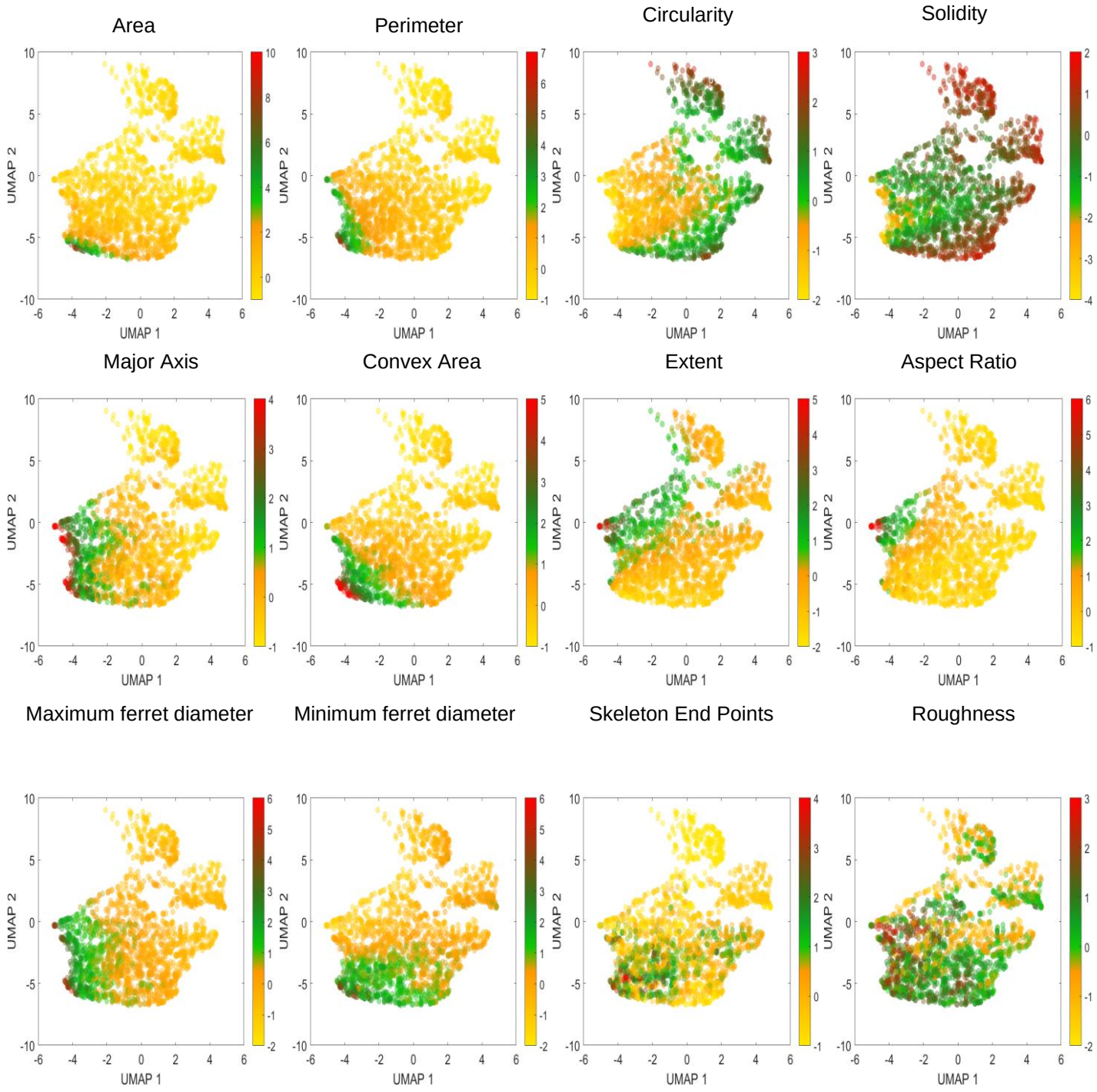

Fig. 3.11: UMAP projections of C2C12 cells on PS dish. Each colorbar indicate the normalized intensity of either Sox2 intensity or the standardized value of each feature.

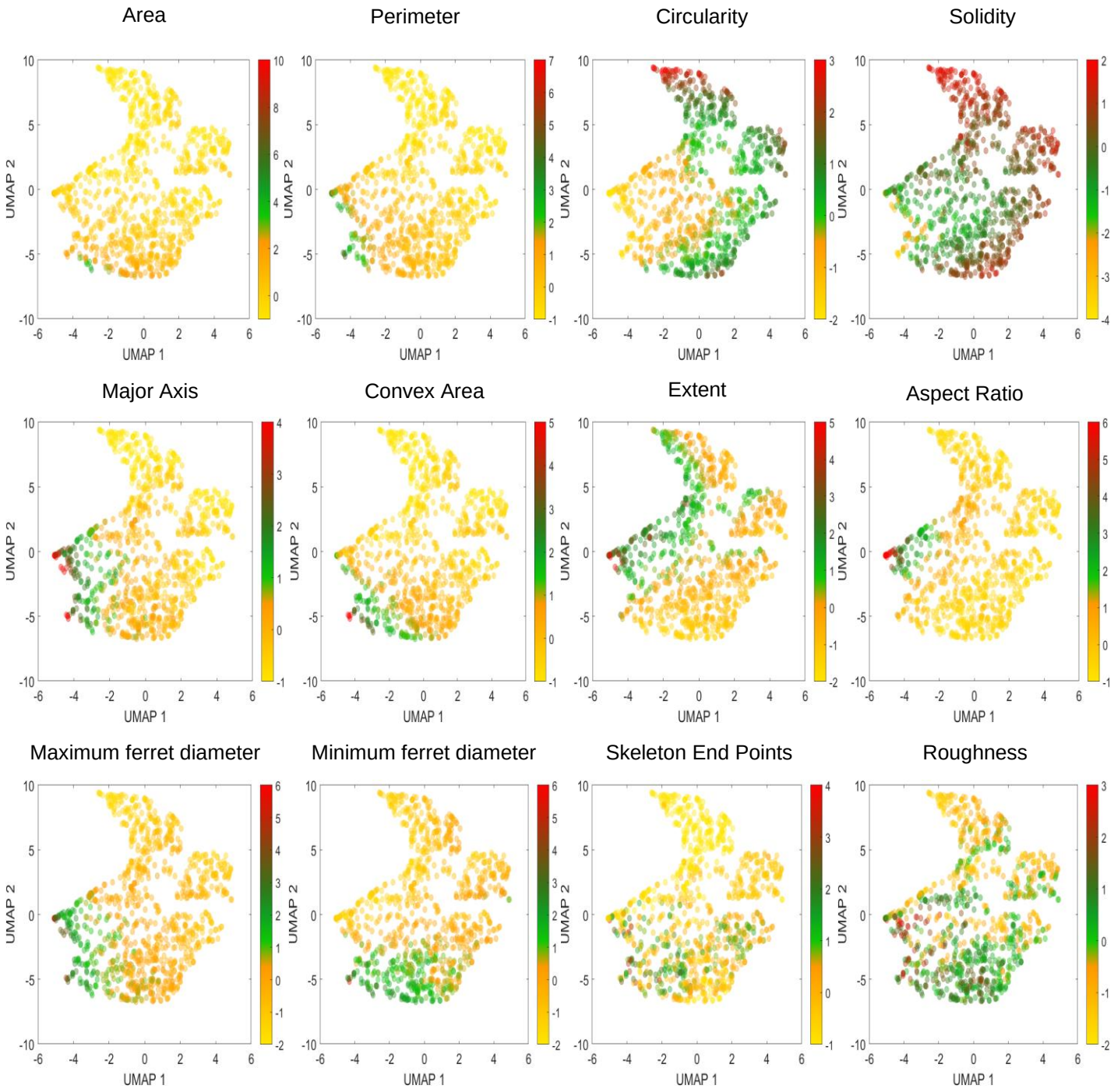

Fig. 3.12: UMAP projections of C2C12 cells on PAMPS gel.

Each colorbar indicate the normalized intensity of either Sox2 intensity or the standardized value of each feature.

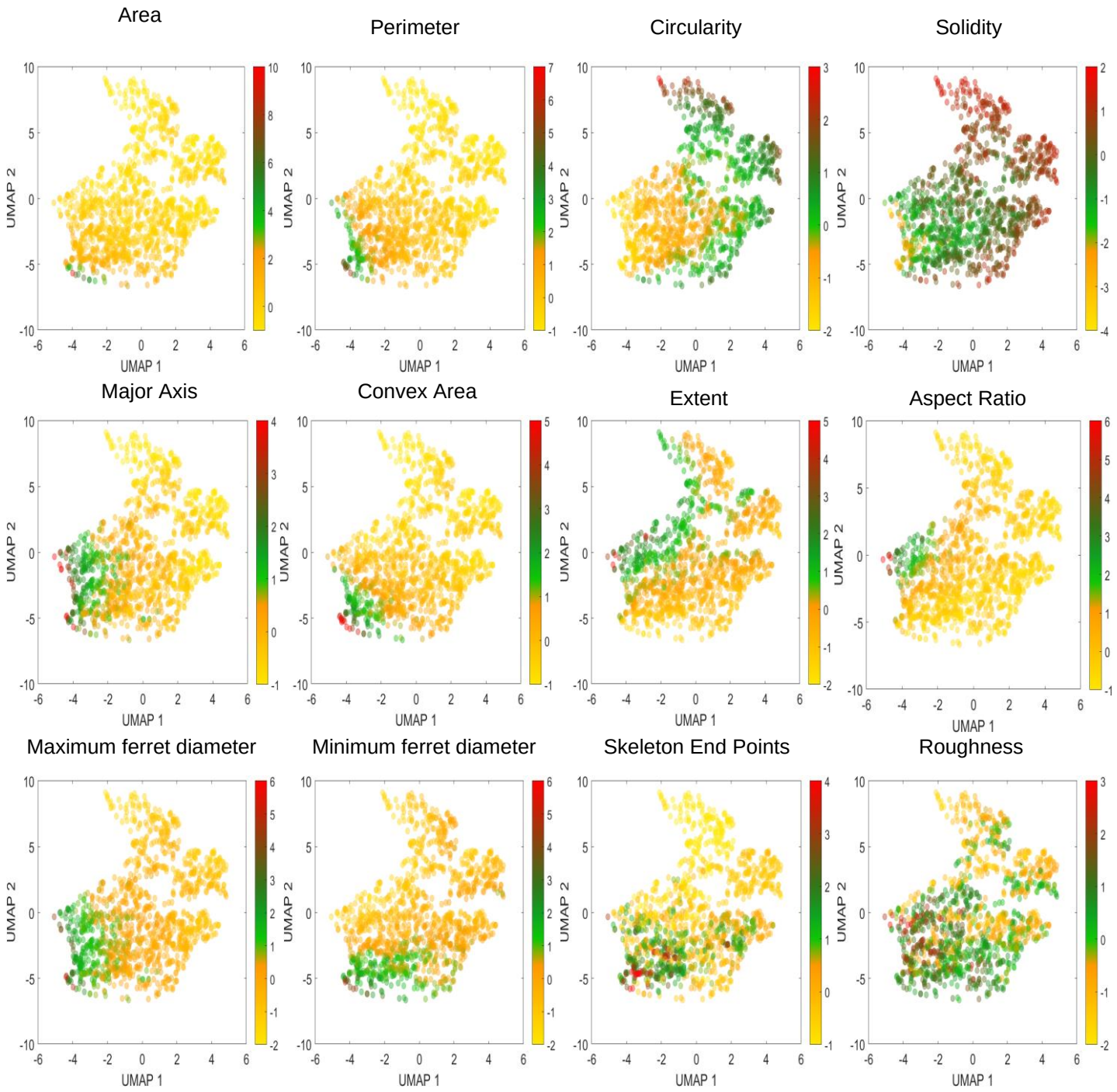

Fig. 3.13: UMAP projections of C2C12 SS18-SSX1 cells on PS dish.

Each colorbar indicate the normalized intensity of either Sox2 intensity or the standardized value of each feature.

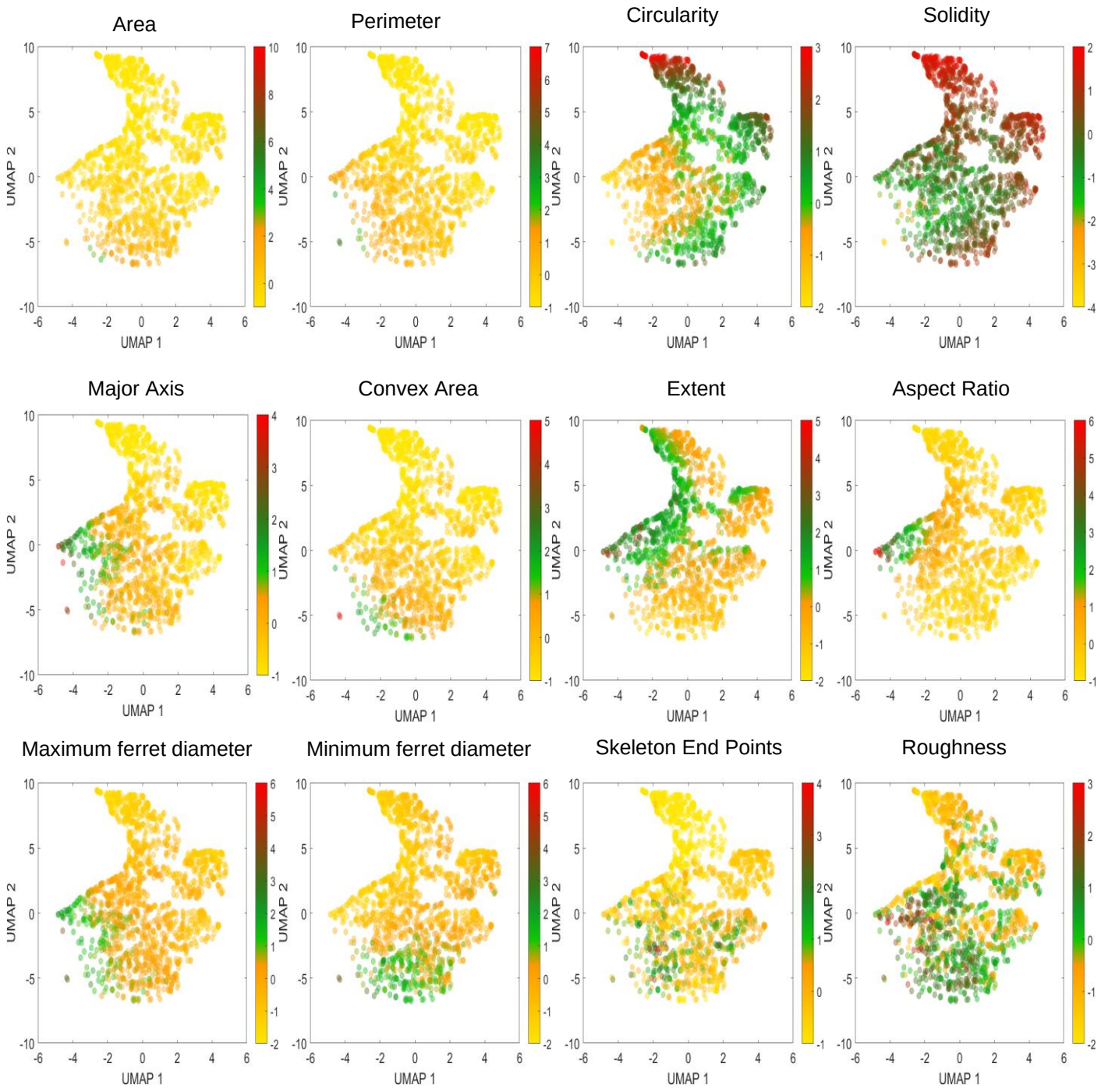

Fig. 3.14: UMAP projections of C2C12 SS18-SSX1 cells on PAMPS dish.

Each colorbar indicate the normalized intensity of either Sox2 intensity or the standardized value of each feature.

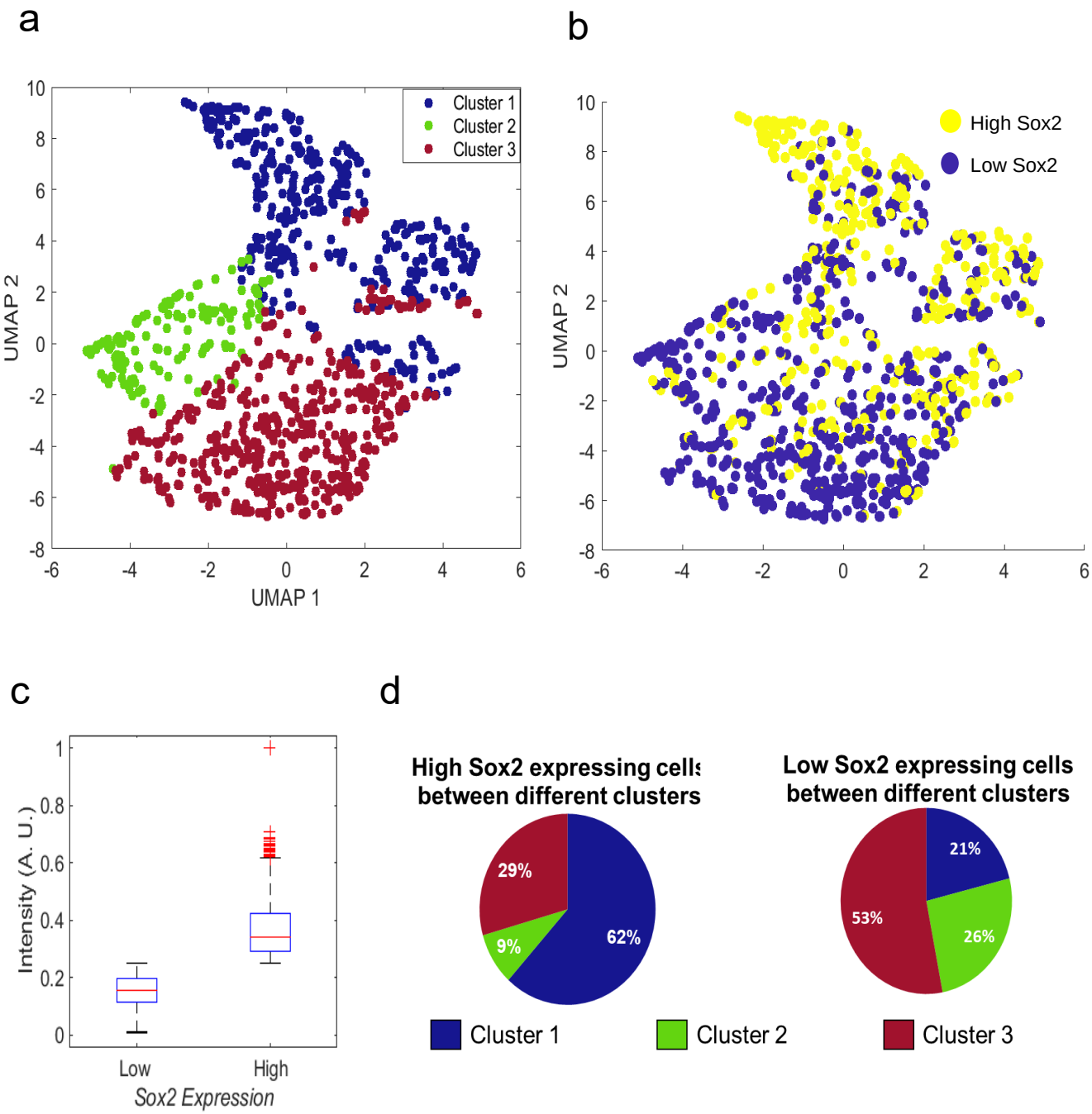

Fig. 3.15: Cluster analysis of C2C12 cells on PAMPS gel.

a. Cluster map of C2C12 cells on PAMPS gel (Using morphological feature) b. Cluster map of C2C12 cells on PAMPS gel (Using Sox2 intensity) c. Distribution of Sox2 intensity in the different d. Percentage of high Sox2 cells and low Sox2 cells in each cluster.

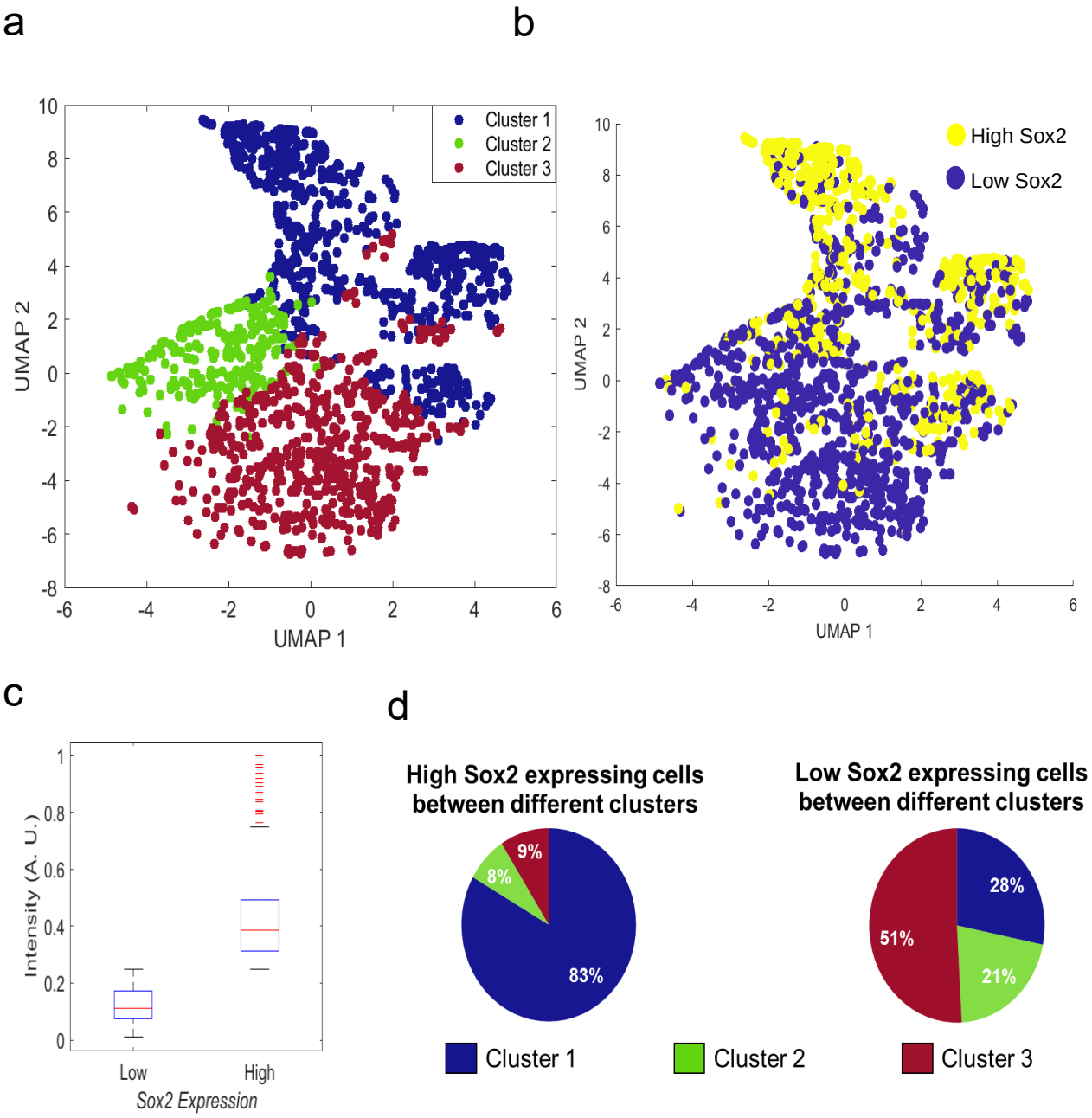

Fig. 3.16: Cluster Analysis of C2C12 SS18-SSX1 cells on PAMPS gel

a. Cluster map of C2C12 SS18-SSX1 cells on PAMPS gel (Using morphological feature) b. Cluster map of C2C12 cells on PAMPS gel (Using Sox2 intensity) c. Distribution of Sox2 intensity in the different clusters, d. Percentage of high Sox2 cells and low Sox2 cells in each cluster.

Chapter 4

Summary
And
Remaining Questions

Summary and remaining questions

Currently, identification of CSCs is difficult because of their scarcity in the entire tumor. However, recent development of biomaterial introduces a new landscape in the field of cancer biology, especially for elucidating CSCs. In this study, we demonstrated that the PAMPS gel could reprogram murine myoblast (C2C12) and C2C12-based synovial sarcoma model cells (C2C12-SS18-SSX1) to the CSC like cells, and our geometrical analysis uncovered the essential morphological features for the CSCs. The reprogramming of cells to CSCs on PAMPS gel allowed us to study their morphology and associated stemness marker (*Sox2*).

Cancer is composed of heterogeneous cell population with different morphological characteristics exhibiting distinct tumorigenicity and metastatic potential. In this study, time-lapse microscopic observation clarified the morphological variety on the PAMPS hydrogel. The large flat cells regularly divided, while the elongated spindle cells moved around vigorously with dynamic morphological changes (Movie 3.1). On the other hand, the small round cells, where morphological feature circularity (F4) and solidity (F5) high, was identified as the hydrogel-induced CSCs (Fig. 3.10). The round cells indicate weak adhesiveness to the PAMPS gel. Adhesion between cells and matrix has been considered to be determined by several mechanisms, such as hydrophobic-dependent adhesion [30], receptor specific binding adhesion such as integrin [31], ionic-dependent adhesion [32], and topological adhesion. We had previously reported that the integrin a4 mediates ATDC5 cell adhesion to the PAMPS gel with anionic sulfate residue leading to chondrogenic differentiation [33]. Therefore, variation in the expression levels of adhesion molecules such as integrin a4 among cell populations may trigger non-uniform adhesiveness to the PAMPS gel, resulting in heterogenous production of the CSCs (Fig. 3.2b).

Meanwhile, on the PAMPS gel, a dense ring-like actin remodeling was occurred in the round cells with high Sox2 expression. These cytoskeletal reconstitutions may lead to the regulation of Hippo signaling pathway. YAP/TAZ are major components of the Hippo signaling, and sense the structural and mechanical features of the cell microenvironment [34]. The YAP/TAZ have been reported to be active in the tumor's CSC fraction, and functionally instrumental and required for CSC expansion [35-39]. In addition, YAP/TAZ have demonstrated to reprogram non-stem tumor cells into cells with full CSC attributes, suggesting that YAP/TAZ may be implicated in the PAMPS gel-induced production of CSCs. Of note, our geometrical analysis clearly demonstrated that the CSCs induced by the PAMPS gel acquired unique morphology like small, rounded shape, whereas no similar morphological features were observed in the CSCs on the PS dish (Fig. 3.3b, 3.3c, 3.4-3.7). As the CSCs present in various tumor microenvironment (designated as niche), such as hypoxic niche [40], perivascular niche [41,42], invasive front niche [43], and immune niche, the PAMPS gel-induced CSCs might induce unique CSCs among them. Combining morphological and gene expression information at the single cell level will reveal the characteristics of the PAMPS gel-induced CSCs, which may unveil clinically and biologically significant features of the CSCs.

Here, the synovial sarcoma model cells (C2C12-SS18-SSX1) demonstrated a higher ability in stemness induction than the wildtype C2C12 cells, which may suggest more poorly differentiated state by SS18-SSX1 oncogene product. Since the SWI/SNF complex including naïve SSX1 has reported to be a mechanoregulated inhibitor of YAP/TAZ [44] and fusion gene-induced stemness was discussed [45,46], the relationship between SS18-SSX1 product and efficiency of stemness induction will be elucidated in the future.

Synovial sarcoma is a high-grade sarcoma [15,16]. Despite the therapeutic advancement, late recurrence more than 10 years after initial treatment may occur [47], indicating the presence of CSCs with dormancy in the surrounding microenvironment for a long time.

$CD133^+$ and aldehyde dehydrogenase 1 $(ALDH1)^{high}$ have been reported to isolate or purify CSCs in synovial sarcoma [48,49]. We also found that CXC-chemokine receptor 4 $(CXCR4)^+$ could be a stem cell marker in this sarcoma [45]. In this study, we incorporated single cell morphological information which is easily measurable to show their morphological heterogeneity with associated stemness related gene expression. Therefore, the gel-based morphological analysis may be a useful tool for rapidly predicting whether patients-derived primary cancer cells are prone to CSCs by seeding them on the hydrogel. In addition, we expect that incorporating bio-chemical characteristics of the CSCs, this could further improve in the development of new diagnostic and therapeutic tool, hopefully to assist in better prognosis of the patients not only the synovial sarcoma but also a lot of types of cancers.

We have previously showed that PAMPS hydrogel can induce CSCs with an elevation of Sox2 expression levels, thus elevation of Sox2 levels is an indicator for CSCs in our system [2]. In addition, we have previously showed that CSCs of synovial sarcoma (SS18-SSX expressing tumor) is highly expressing Sox2 [45]. Thus, we believe that Sox2-high cells are CSCs. Based on our previous studies and current ongoing study, we have found that the endogenous expression levels of Nanog and OCT 3/4 were extremely low compared to the SOX2 even on the hydrogel [2], and they were undetectable in immunofluorescence of this study.

On the other hand, one of the most reliable functional assays for CSCs is measurement of in vivo tumor forming potential, and for this assay we found that we need at least two weeks of culture on gel. In fact, we successfully proved that an injection of very small number of 500 cells into mice clearly generated tumor in mice and concluded that the hydrogel appropriately generates CSCs [2]. We also confirmed that in case of 3 days of gel culture, co-injection of particle hydrogel with the CSCs needed to form tumor in vivo [2]. Thus, we have already extensively analyzed the potential of the hydrogels induced CSCs. On the other hand, because

the main purpose of this study is rapid prediction of CSCs within 3 days on hydrogels, thereby we did not perform in vivo tumor forming assay in this study, which might be the limitation of this study. The establishment of the rapid prediction system is expected to contribute to the clinical prediction of the presence of CSCs in the surgical/biopsy specimens for cancer patients in the future.

References

[1] Chaffer CL, Weinberg RA, A perspective on cancer cell metastasis, Science. 331 (2011) 559–564.

[2] J. Suzuka, M. Tsuda, L. Wang, S. Kohsaka, K. Kishida, S. Semba, H. Sugino, S. Aburatani, M. Frauenlob, T. Kurokawa, S. Kojima, T. Ueno, Y. Ohmiya, H. Mano, K. Yasuda, J.P. Gong, S. Tanaka, Rapid reprogramming of tumour cells into cancer stem cells on double-network hydrogels, Nat Biomed Eng 5 (2021) 914-925. doi: 10.1038/s41551-021-00692-2.

[3] Toepfner N, Herold C, Otto O. et al., Detection of human disease conditions by single-cell morpho-rheological phenotyping of blood. Elife. 13 (2018) e29213. doi: 10.7554/eLife.29213.

[4] Cooper LA, Kong J, Gutman DA, Wang F, Gao J, Appin C, Cholleti S, Pan T, Sharma A, Scarpace L, Mikkelsen T, Kurc T, Moreno CS, Brat DJ, Saltz JH, Integrated morphologic analysis for the identification and characterization of disease subtypes. J Am Med Inform Assoc, 19 (2012) 317-323. doi: 10.1136/amiajnl-2011-000700.

[5] Yeung, T. et al. Effects of substrate stiffness on cell morphology, cytoskeletal structure, and adhesion. Cell Motil Cytoskeleton. 60 (2005) 24-34. doi: 10.1002/cm.20041.

[6] Kamada R, Tano F, Kudoh F, Kimura N, Chuman Y, Osawa A, et al. Effective Cellular Morphology Analysis for Differentiation Processes by a Fluorescent 1,3a,6a-Triazapentalene Derivative Probe in Live Cells. PLoS ONE 11((2016)) e0160625. doi: 10.1371/journal.pone.0160625

[7] Da, Q., Deng, S., Li, J. et al. Quantifying the cell morphology and predicting biological behavior of signet ring cell carcinoma using deep learning. Sci Rep 12, 183 (2022). doi: 10.1038/s41598-021-03984-4

[8] Wali, G., Berkovsky, S., Whiten, D.R. et al. Single cell morphology distinguishes genotype and drug effect in Hereditary Spastic Paraplegia. Sci Rep 11, 16635 (2021). doi: 10.1038/s41598-021-95995-4

[9] C. Bakal, J. Aach, G. Church, N. Perrimon, Quantitative morphological signatures define local signaling networks regulating cell morphology. *Science* 316 (2007) 1753–1756.

[10] Ying Li, Jianglei Di, Kaiqiang Wang, Sufang Wang, and Jianlin Zhao, Classification of cell morphology with quantitative phase microscopy and machine learning, Opt. Express 28 (2020) 23916-23927.

[11] Mousavikhamene, Z., Sykora, D.J., Mrksich, M. et al. Morphological features of single cells enable accurate automated classification of cancer from non-cancer cell lines. Sci Rep 11 (2021) 24375. doi: 10.1038/s41598-021-03813-8

[12] P.-H. Wu, D.M. Gilkes, J.M. Phillip, A. Narkar, T.W.-T. Cheng, J. Marchand, M.-H. Lee, R. Li, D. Wirtz, Single-cell morphology encodes metastatic potential, Sci Adv. 6 (2020) eaaw6938. doi: 10.1126/sciadv.aaw6938.

[13] Harkness L, Chen X, Gillard M, Gray PP, Davies AM, Media composition modulates human embryonic stem cell morphology and may influence preferential lineage differentiation potential. PLoS ONE 14(2019): e0213678. doi: 10.1371/journal.pone.0213678

[14] Rowena McBeath, Dana M Pirone, Celeste M Nelson, Kiran Bhadriraju, Christopher S Chen, Cell Shape, Cytoskeletal Tension, and RhoA Regulate Stem Cell Lineage Commitment, Developmental Cell, 6 (2004) 483-495. Doi: 10.1016/s1534-5807(04)00075-9.

[15] Herzog CE. Overview of sarcomas in the adolescent and young adult population. J Pediatr Hematol Oncol, 27 (2005) 215-218. doi: 10.1097/01.mph.0000161762.53175.e4.

[16] Sultan I, Rodriguez-Galindo C, Saab R, Yasir S, Casanova M, Ferrari A. Comparing children and adults with synovial sarcoma in the Surveillance, Epidemiology, and End Results program, 1983 to 2005: an analysis of 1268 patients. Cancer 115 (2009) 3537-3547. doi: 10.1002/cncr.24424.

[17] Davis SR, Meltzer PS. Modeling synovial sarcoma: timing is everything. Cancer Cell. 11 (2007) 305-307. doi: 10.1016/j.ccr.2007.03.016.

[18] de Bruijn DR, Allander SV, van Dijk AH, Willemse MP, Thijssen J, van Groningen JJ, Meltzer PS, van Kessel AG. The synovial-sarcoma-associated SS18-SSX2 fusion protein induces epigenetic gene (de)regulation. Cancer Res, 66 (2006) 9474-9482.

[19] Su L, Sampaio AV, Jones KB, Pacheco M, Goytain A, Lin S, Poulin N, Yi L, Rossi FM, Kast J, and others. Deconstruction of the SS18-SSX fusion oncoprotein complex: insights into disease etiology and therapeutics. Cancer Cell, 21(2012) 333-347. doi: 10.1016/j.ccr.2012.01.010.

[20] Jones KB, Su L, Jin H, Lenz C, Randall RL, Underhill TM, Nielsen TO, Sharma S, Capecchi MR. SS18-SSX2 and the mitochondrial apoptosis pathway in mouse and human synovial sarcomas. Oncogene 32(2013) 2365-71, 2375.e1-5. doi: 10.1038/onc.2012.247.

[21] Kadoch C, Hargreaves DC, Hodges C, Elias L, Ho L, Ranish J, Crabtree GR. Proteomic and bioinformatic analysis of mammalian SWI/SNF complexes identifies extensive roles in human malignancy. Nat Genet 45 (2013) 592-601. doi: 10.1038/ng.2628.

[22] Kadoch C, Crabtree GR. Reversible disruption of mSWI/SNF (BAF) complexes by the SS18-SSX oncogenic fusion in synovial sarcoma. Cell 153(2013) 71-85. doi: 10.1016/j.cell.2013.02.036.

[23] McBride MJ, Pulice JL, Beird HC, Ingram DR, D'Avino AR, Shern JF, Charville GW, Hornick JL, Nakayama RT, Garcia-Rivera EM and others. The SS18-SSX Fusion Oncoprotein Hijacks BAF Complex Targeting and Function to Drive Synovial Sarcoma. Cancer Cell 33 (2018) 1128-1141.e7. doi: 10.1016/j.ccell.2018.05.002.

[24] Hyuck Joon Kwon, Kazunori Yasuda, Yoshihiro Ohmiya, Ken-ichi Honma, Yong Mei Chen, Jian Ping Gong. In vitro differentiation of chondrogenic ATDC5 cells is enhanced by culturing on synthetic hydrogels with various charge densities. Acta Biomater 6 (2010) 494-501. doi: 10.1016/j.actbio.2009.07.033.

[25] Bhaskar, Dhananjay, Lee, Darrick, Knútsdóttir, Hildur, Tan, Cindy, Zhang, MoHan, Dean, Pamela, Roskelley, Calvin, Edelstein-Keshet, Leah. A methodology for morphological feature extraction and unsupervised cell classification. (2019). 10.1101/623793.

[26] Lobo J, See EY, Biggs M, Pandit A. An insight into morphometric descriptors of cell shape that pertain to regenerative medicine. J Tissue Eng Regen Med. 10 (2016) 539-553. doi: 10.1002/term.1994.

[27] https://arxiv.org/abs/1802.03426

[28] Goodfellow, I., Bengio, Y., and Courville, A. (2016). Deep Learning (MIT Press).

[29] Eric M. Christiansen, Samuel J. Yang, D. et.al. In Silico Labeling: Predicting Fluorescent Labels in Unlabeled Images, Cell, Volume 173, Issue 3, 2018, Pages 792-803.e19, ISSN 0092-8674, https://doi.org/10.1016/j.cell.2018.03.040.

[30] T Matsuda, T Sugawara. Development of surface photochemical modification method for micropatterning of cultured cells. J Biomed Mater Res. 29 (1995) 749-756. doi: 10.1002/jbm.820290611.

[31] Benjamin Geiger, Joachim P Spatz, Alexander D Bershadsky. Environmental sensing through focal adhesions. Nat Rev Mol Cell Biol. 10 (2009) 21-33. doi:10.1038/nrm2593.

[32] Stéphanie Le Clair, Khoi Nguyen, and Zhan Chen. Sum Frequency Generation Studies on Bioadhesion: Elucidating the Molecular Structure of Proteins at Interfaces. J Adhes. 85 (2009) 484–511.

[33] Daiki Hashimoto, Shingo Semba, Masumi Tsuda, Takayuki Kurokawa, Nobuto Kitamura, Kazunori Yasuda, Jian Ping Gong, Shinya Tanaka. Integrin α4 mediates ATDC5 cell adhesion to negatively charged synthetic polymer hydrogel leading to chondrogenic differentiation. Biochem Biophys Res Commun. 528 (2020) 120-126. doi: 10.1016/j.bbrc.2020.05.071.

[34] Zanconato F, Cordenonsi M, Piccolo S. YAP/TAZ at the Roots of Cancer. Cancer Cell. 29 (2016) 783-803. doi: 10.1016/j.ccell.2016.05.005.

[35] M Bartucci, R Dattilo, C Moriconi, A Pagliuca, M Mottolese, G Federici, A Di Benedetto, M Todaro, G Stassi, F Sperati, M I Amabile, E Pilozzi, M Patrizii, M Biffoni, M Maugeri-Saccà, S Piccolo, R De Maria. TAZ is required for metastatic activity and chemoresistance of breast cancer stem cells. Oncogene. 34 (2015) 681-90. doi: 10.1038/onc.2014.5.

[36] Upal Basu-Roy, N Sumru Bayin, Kirk Rattanakorn, Eugenia Han, Dimitris G Placantonakis, Alka Mansukhani, Claudio Basilico. Sox2 antagonizes the Hippo pathway to maintain stemness in cancer cells. Nat Commun. 6 (2015) 6411. doi: 10.1038/ncomms7411.

[37] Michelangelo Cordenonsi, Francesca Zanconato, Luca Azzolin, Mattia Forcato, Antonio Rosato, Chiara Frasson, Masafumi Inui, Marco Montagner, Anna R Parenti, Alessandro Poletti, Maria Grazia Daidone, Sirio Dupont, Giuseppe Basso, Silvio Bicciato, Stefano Piccolo. The Hippo transducer TAZ confers cancer stem cell-related traits on breast cancer cells. Cell. 147 (2011) 759-772. doi: 10.1016/j.cell.2011.09.048.

[38] Hiromitsu Hayashi, Takaaki Higashi, Naomi Yokoyama, Takayoshi Kaida, Keita Sakamoto, Yukiko Fukushima, Takatsugu Ishimoto, Hideyuki Kuroki, Hidetoshi Nitta, Daisuke Hashimoto, Akira Chikamoto, Eiji Oki, Toru Beppu, Hideo Baba. An Imbalance in TAZ and YAP Expression in Hepatocellular Carcinoma Confers Cancer Stem Cell-like Behaviors Contributing to Disease Progression. Cancer Res. 75 (2015) 4985-4997. doi: 10.1158/0008-5472.CAN-15-0291.

[39] Shumei Song, Jaffer A Ajani, Soichiro Honjo, Dipen M Maru, Qiongrong Chen, Ailing W Scott, Todd R Heallen, Lianchun Xiao, Wayne L Hofstetter, Brian Weston, Jeffrey H Lee, Roopma Wadhwa, Kazuki Sudo, John R Stroehlein, James F Martin, Mien-Chie Hung, Randy L Johnson. Hippo coactivator YAP1 upregulates SOX9 and endows esophageal cancer cells with stem-like properties. Cancer Res. 74 (2014) 4170-4182. doi: 10.1158/0008-5472.CAN-13-3569.

[40] Satoru Osuka, Erwin G Van Meir. Overcoming therapeutic resistance in glioblastoma: the way forward. J Clin Invest. 127 (2017) 415-426. doi: 10.1172/JCI89587.

[41] Richard J Gilbertson, Jeremy N Rich. Making a tumour's bed: glioblastoma stem cells and the vascular niche. Nat Rev Cancer. 7 (2007) 733-736. doi: 10.1038/nrc2246.

[42] Jason M Butler, Hideki Kobayashi, Shahin Rafii. Instructive role of the vascular niche in promoting tumour growth and tissue repair by angiocrine factors. Nat Rev Cancer. 10 (2010) 138-146. doi: 10.1038/nrc2791.

[43] Yoshida GJ. The heterogeneity of cancer stem-like cells at the invasive front. Cancer Cell Int. 17 (2017) 23. doi: 10.1186/s12935-017-0393-y.

[44] Chang L, Azzolin L, Di Biagio D, Zanconato F, Battilana G, Lucon Xiccato R, Aragona M, Giulitti S, Panciera T, Gandin A, Sigismondo G, Krijgsveld J, Fassan M, Brusatin G,

Cordenonsi M, Piccolo S. The SWI/SNF complex is a mechanoregulated inhibitor of YAP and TAZ. Nature. 563 (2018) 265-269. doi: 10.1038/s41586-018-0658-1.

[45] Kimura T, Wang L, Tabu K, Tsuda M, Tanino M, Maekawa A, Nishihara H, Hiraga H, Taga T, Oda Y, and others. Identification and analysis of CXCR4-positive synovial sarcoma-initiating cells.

[46] Panicker S, Venkatabalasubramanian S, Pathak S, Ramalingam S. The impact of fusion genes on cancer stem cells and drug resistance. Mol Cell Biochem 476 (2021) 3771-3783. doi: 10.1007/s11010-021-04203-4.

[47] Krieg AH, Hefti F, Speth BM, Jundt G, Guillou L, Exner UG, von Hochstetter AR, Cserhati MD, Fuchs B, Mouhsine E, and others. Synovial sarcomas usually metastasize after >5 years: a multicenter retrospective analysis with minimum follow-up of 10 years for survivors. Ann Oncol 22 (2011) 458-467. doi: 10.1093/annonc/mdq394.

[48] Terry J, Nielsen T. Expression of CD133 in synovial sarcoma. Appl Immunohistochem Mol Morphol 18 (2010)159-65. doi: 10.1097/PAI.0b013e3181b77451.

[49] Lohberger B, Rinner B, Stuendl N, Absenger M, Liegl-Atzwanger B, Walzer SM, Windhager R, Leithner A. Aldehyde dehydrogenase 1, a potential marker for cancer stem cells in human sarcoma. PLoS One 7 (2012) e43664. doi: 10.1371/journal.pone.0043664.